ARTICLES
https://doi.org/10.1038/s41588-019-0412-0
nature genetics

The bipartite TAD organization of the X-inactivation center ensures opposing developmental regulation of *Tsix* and *Xist*

Joke G. van Bemmel[1,2,14,16*], Rafael Galupa[1,15,16], Chris Gard[1], Nicolas Servant[3,4], Christel Picard[1], James Davies[5], Anthony James Szempruch[6], Yinxiu Zhan[7,8], Jan J. Żylicz[1,9], Elphège P. Nora[10], Sonia Lameiras[11], Elzo de Wit[12], David Gentien[13], Sylvain Baulande[11], Luca Giorgetti[7], Mitchell Guttman[6], Jim R. Hughes[5], Douglas R. Higgs[5], Joost Gribnau[2] and Edith Heard[1*]

The mouse X-inactivation center (*Xic*) locus represents a powerful model for understanding the links between genome architecture and gene regulation, with the non-coding genes *Xist* and *Tsix* showing opposite developmental expression patterns while being organized as an overlapping sense/antisense unit. The *Xic* is organized into two topologically associating domains (TADs) but the role of this architecture in orchestrating *cis*-regulatory information remains elusive. To explore this, we generated genomic inversions that swap the *Xist/Tsix* transcriptional unit and place their promoters in each other's TAD. We found that this led to a switch in their expression dynamics: *Xist* became precociously and ectopically upregulated, both in male and female pluripotent cells, while *Tsix* expression aberrantly persisted during differentiation. The topological partitioning of the *Xic* is thus critical to ensure proper developmental timing of X inactivation. Our study illustrates how the genomic architecture of *cis*-regulatory landscapes can affect the regulation of mammalian developmental processes.

Spatiotemporal regulation of gene expression during mammalian development often involves distal *cis*-regulatory elements, which can be located tens to hundreds of kilobases (kb) away from their target genes (reviewed in ref. [1]). Dynamic interactions between enhancers and their target promoters preferentially occur inside the 200 kb to 1 megabase (Mb) topologically associating domains (TADs)[2,3], within which smaller self-interacting domains can form[4,5]. TADs represent a functionally privileged scale in the hierarchical folding of chromosomes[6], and are largely conserved across cell types and species[2,7], in contrast to smaller self-interacting domains. Transcription within TADs is often co-regulated[3,8] and most enhancer–promoter pairs reside within the same TAD[6,9,10]. TADs are frequently delimited by genomic sites bound by CCCTC-binding factor (CTCF) and cohesin[2,4,6,11], both of which have been shown to contribute to TAD organization[4,5,12–14]. Genetic alterations of CTCF-binding sites (CBSs) have shown that the genomic location and orientation of CBSs can determine the directionality of long-range interactions and TAD organization[15–21]. However, the functional relationship between TADs, their boundaries and transcriptional regulation remains unclear.

Here we used the X-inactivation center (*Xic*), a model of developmentally regulated loci with complex *cis*-regulatory landscapes, to understand how genomic architecture might affect transcriptional regulation. The *Xic* is required for the initiation of X-chromosome inactivation (XCI) in female mammals[22–25]. It harbors both *Xist*, the locus producing the key long non-coding RNA (lncRNA) that triggers XCI, and its antisense transcription unit, *Tsix*. *Xist* becomes mono-allelically upregulated at the onset of XCI and its lncRNA coats the future inactive X chromosome in *cis* and triggers its silencing. *Tsix* is transcribed antisense to *Xist* and represses *Xist* expression during differentiation (reviewed in ref. [26]). The developmental regulation of *Xist* and *Tsix* during random XCI can be explored using mouse embryonic stem cells (mESCs). In pluripotent male and female mESCs, *Tsix* is robustly expressed, while *Xist* is barely transcribed[27–29]. Differentiation of mESCs is associated with downregulation of *Tsix* and the activation of *Xist* expression, which is very transient in males[29], and more robust and long-lasting in females, presumably due to a double dose of X-linked factors (reviewed in ref. [26]). *Tsix* expression during early differentiation is believed to contribute to the mono-allelic regulation of *Xist* in female differentiating mESCs[30]. Initially, *Tsix* is highly expressed from both X chromosomes; during differentiation it becomes repressed on the future inactive X (expressing *Xist*) and remains transcribed only from the future active X[31–33]. In summary, *Xist* and *Tsix* adopt

[1]Institut Curie, CNRS UMR3215, INSERM U934, Paris, France. [2]Department of Developmental Biology, Erasmus Medical Center Rotterdam (EMC), Rotterdam, the Netherlands. [3]Institut Curie, PSL Research University, INSERM, U900, Paris, France. [4]MINES ParisTech, PSL Research University, CBIO-Centre for Computational Biology, Paris, France. [5]Medical Research Council, Molecular Haematology Unit, Weatherall Institute of Molecular Medicine, University of Oxford, John Radcliffe Hospital, Oxford, UK. [6]Division of Biology and Biological Engineering, California Institute of Technology, Pasadena, CA, USA. [7]Friedrich Miescher Institute for Biomedical Research, Basel, Switzerland. [8]University of Basel, Basel, Switzerland. [9]University of Cambridge, Department of Physiology, Development and Neuroscience, Cambridge, UK. [10]Gladstone Institute of Cardiovascular Disease and Roddenberry Center for Stem Cell Biology and Medicine at Gladstone, San Francisco, CA, USA. [11]Institut Curie Genomics of Excellence (ICGex) Platform, Institut Curie Research Center, Paris, France. [12]Oncode Institute and Division of Gene Regulation, the Netherlands Cancer Institute, Amsterdam, the Netherlands. [13]Institut Curie, PSL Research University, Translational Research Department, Genomics Platform, Paris, France. [14]Present address: Gladstone Institute of Cardiovascular Diseases, San Francisco, CA, USA. [15]Present address: European Molecular Biology Laboratory, Heidelberg, Germany. [16]These authors contributed equally: Joke G. van Bemmel, Rafael Galupa. *e-mail: jokevbemmel@gmail.com; edith.heard@curie.fr

opposite transcriptional fates during mESC differentiation, despite their overlapping transcriptional units. Their promoters lie in separate, adjacent TADs[3] (Fig. 1a–c). The TAD containing the *Xist* promoter (named TAD-E[3], ~550 kb) also includes several coding (for example, *Rnf12*) and non-coding sequences (for example, *Jpx*, *Ftx*) reported to regulate *Xist*[34–36]; likewise, the TAD harboring the *Tsix* promoter (named TAD-D[3], ~250 kb) also contains putative *Tsix cis*-regulators (for example, *Xite*, *Linx*)—reviewed in refs. [26,37–39]. The opposite transcriptional fates of *Xist* and *Tsix* during differentiation are coordinated with those of the other loci within their respective TADs[3]. This bipartite organization of the *Xic* into two TADs has thus been proposed to separate the *Xist*/*Tsix* regulatory landscapes and to promote coordinated expression of the genes in each TAD. However, whether appropriate *Xist* and *Tsix* regulation does require such partitioning of the promoters from each other within separate TADs remains unknown. Here, we explore the extent to which TAD environments can have an impact on accurate gene regulation by generating genomic inversions that swap the *Xist* and *Tsix* promoters between neighboring TADs and assessing the degree to which three-dimensional organization, appropriate gene regulation and XCI timing are affected.

Results

Genomic inversions involving the *Xist*/*Tsix* transcriptional unit place their promoters into each other's TADs. We designed and generated a genomic inversion of the *Xist*/*Tsix* locus (~40 kb), including their respective promoters, in male mESCs (see Methods for a detailed description and Fig. 1d and Supplementary Fig. 1a). To investigate whether this inversion switches the topological environment of the *Xist* and *Tsix* promoters, we used Capture-C[40,41] to obtain high-resolution interaction profiles for their transcription start sites (TSS) in both wild type and inverted alleles (Fig. 1e for clone no. 1, Supplementary Fig. 2c for clone no. 2 and Fig. 1c for Capture-C viewpoints). In wild type cells, the interaction profiles clearly reflected the presence of the two TADs: the *Tsix* promoter preferentially interacted with sequences within TAD-D, while the *Xist* promoter preferentially interacted with sequences within TAD-E. In cells harboring the 40-kb [*Tsix-Xist*] inversion, the interaction profiles of the promoters switched: the *Tsix* promoter preferentially interacted with sequences within TAD-E (70% in inversion versus 30% in wild type, averages), while the *Xist* promoter preferentially interacted within TAD-D (71% in inversion versus 40% in wild type, averages) (Fig. 1e, Supplementary Fig. 2c and Supplementary Fig. 2f for visual comparison of the wild type and inverted alleles). Modeling of the background contact probabilities at either side of the viewpoints, before and after inversion, confirmed that the promoters switched their interaction preferences from one TAD to the other (Supplementary Fig. 2g). To evaluate the structure of the TADs in the inverted allele, we then performed 5C (chromosome conformation capture carbon-copy[42]) across a 4.5-Mb region centered on *Xist* (as before, ref. [3]). The 5C interaction profile of the inverted allele was very similar to that of the wild type, based on differential maps and insulation scores (Fig. 1f–h for clone no. 1 and Supplementary Fig. 3c–e for clone no. 2). We thus successfully placed the *Xist* and *Tsix* promoters in each other's TADs, without compromising the insulation between the TADs or changing the overall TAD structure. The overall absence of changes in TAD structure is consistent with models of CTCF-mediated loops (reviewed in ref. [43]), given that the CBS configuration between the wild type and inverted alleles is equivalent (compare Fig. 1c,d). Together, our results reveal that the promoters of *Xist* and *Tsix*, when inverted, switch their interaction preference, losing to some extent their original interactions, and adopting interactions predominantly within the new TADs in which they lie. Our 40-kb inversion therefore allows us to investigate the consequences of changing the topological and *cis*-regulatory environment of a promoter.

We also designed and generated a second inversion in male mESCs spanning a 70-kb region including not only *Xist* and *Tsix* but also their immediately adjacent loci, *Jpx* and *Xite* (see Methods for a detailed description and Fig. 2a and Supplementary Fig. 1). *Xite* is a reported enhancer of *Tsix*[44,45], while *Jpx* is co-expressed with *Xist* during differentiation[34], and has been reported to activate *Xist*, either in *cis*[46], in *trans*[34,47] or both[48]. We performed Capture-C for the TSSs of *Xist* and *Tsix* in male mESCs harboring the 70-kb [*Xite-Jpx*] inversion and found that, similarly to the 40-kb [*Tsix-Xist*] inversion, the interaction profiles for both *Tsix* and *Xist* promoters were switched when compared to wild type (Fig. 2b for clone no. 1 and Supplementary Fig. 2d for clone no. 2). To investigate the new interactomes in the 70-kb inversion in more detail, we performed Capture-C for *Xite* (overlapping CBS no. 2) or *Jpx* TSS (Fig. 2c for clone no. 1, Supplementary Fig. 2e for clone no. 2 and Fig. 1c for Capture-C viewpoints). In wild type cells, *Xite's* interactions are predominantly within TAD-D (85%, average), showing particularly strong interactions with *Linx* and *Chic1*, as previously reported[3,49]. The TSS of *Jpx* has an interaction profile mostly restricted to TAD-E (72%, average). In cells harboring the 70-kb [*Xite-Jpx*] inversion, both *Xite* and *Jpx* showed preferential interactions within the new TAD each now lies in (83 and 72%, respectively). We found that *Xite* no longer interacted with *Linx* and *Chic1* and instead displayed strong interactions within TAD-E, whereas *Jpx* showed a fairly

Fig. 1 | Genomic inversion of the *Xist*/*Tsix* loci switches their promoters into each other's original TADs. a, Schematic illustration of the *Xic* organized into two TADs. Red (TAD-D) and blue (TAD-E) shaded circles represent the interaction environments of *Tsix* and *Xist*. Dashed arrows indicate *cis*-activation. Black arrow from *Rnf12* indicates *trans*-activation by the protein RNF12 (orange circles). Dashed line from *Tsix* to *Xist* indicates antisense repression. **b**, Linear visualization of the *Xic* organized into two TADs. Dashed box represents the previously described 68-kb boundary deletion[3]. TADs determined using the insulation score, are depicted as colored bars (red, blue, gray). Dotted lines at start of TAD-D indicate undefined TAD structure due to repetitive sequences. CBSs in forward (blue) and reverse (red) orientation, and CTCF ChIP–sequencing signal in E14 mESCs[14]. Gene annotation from UCSC RefSeq mm9 (ref. [61]), except for *Xite* (see Methods) and *Linx*[3]. **c**, Schematic representation of boundary region and its CBSs in male mESCs. Probes for capture enrichment (viewpoint) depicted with black arrowheads. On the right, 5C chromosome conformation contact frequencies in wild type male mESCs. Map represents normalized and binned pool of two samples. **d**, Schematic representation of the 40-kb [*Tsix-Xist*] inversion in male mESCs. Blue shaded box indicates inverted region. **e**, Capture-C profiles for *Tsix* (red) and *Xist* (blue) viewpoints depicting normalized interaction frequencies per 10,000 (10 k) total interactions within the analyzed region (see Methods), in wild type and 40-kb [*Tsix-Xist*] inversion. Viewpoints depicted with black arrowheads. Underneath, forward CBSs in blue, reverse CBSs in red and genes as colored boxes as in **a**, forward-oriented genes above and reverse-oriented genes below the gray line. Differential interaction frequencies of wild type minus inversion interaction frequencies in black (interaction gain) and gray (interaction loss). Relative percentage of normalized interactions on either side of the viewpoints is indicated (see Methods). **f**, 5C chromosome conformation contact frequencies in male mESCs harboring a 40-kb [*Tsix-Xist*] inversion; map represents inverted genome. Pool of two normalized and binned replicates, as in **c**. **g**, Differential map represents subtraction of wild type from inversion *Z*-scores. Gray pixels correspond to filtered interactions that did not meet the quality control threshold. **h**, Insulation scores, wild type in black and 40-kb [*Tsix-Xist*] inversion in red. Inverted region represented by light blue box. Chromosome positions are aligned with **f** and **g**. Note that each genomic alteration has been generated twice (two independent cell lines). Results for the first clone are shown here, results for the second clone are shown in Supplementary Figs. 2 and 3.

flat profile of interactions, nevertheless restricted to TAD-D. To evaluate the structure of the TADs in the 70-kb inverted allele, we performed 5C and observed specific changes (Fig. 2e–g for clone no. 1, Supplementary Fig. 3c–e for clone no. 2). In particular, there was a localized loss of structure within TAD-D, when comparing the 70-kb inversion to wild type (black arrowheads in Fig. 2e,f). This corresponded to interactions established by *Xite* in the wild type, and by *Jpx* in the inverted allele, indicating that *Jpx* is unable to replace *Xite* original interactions, as already suggested by Capture-C (Fig. 2c,d). We also observed a localized gain of interactions (a 'flame') within TAD-E (green arrowheads in Fig. 2e,f). These are ectopic interactions between *Xite* and sequences within

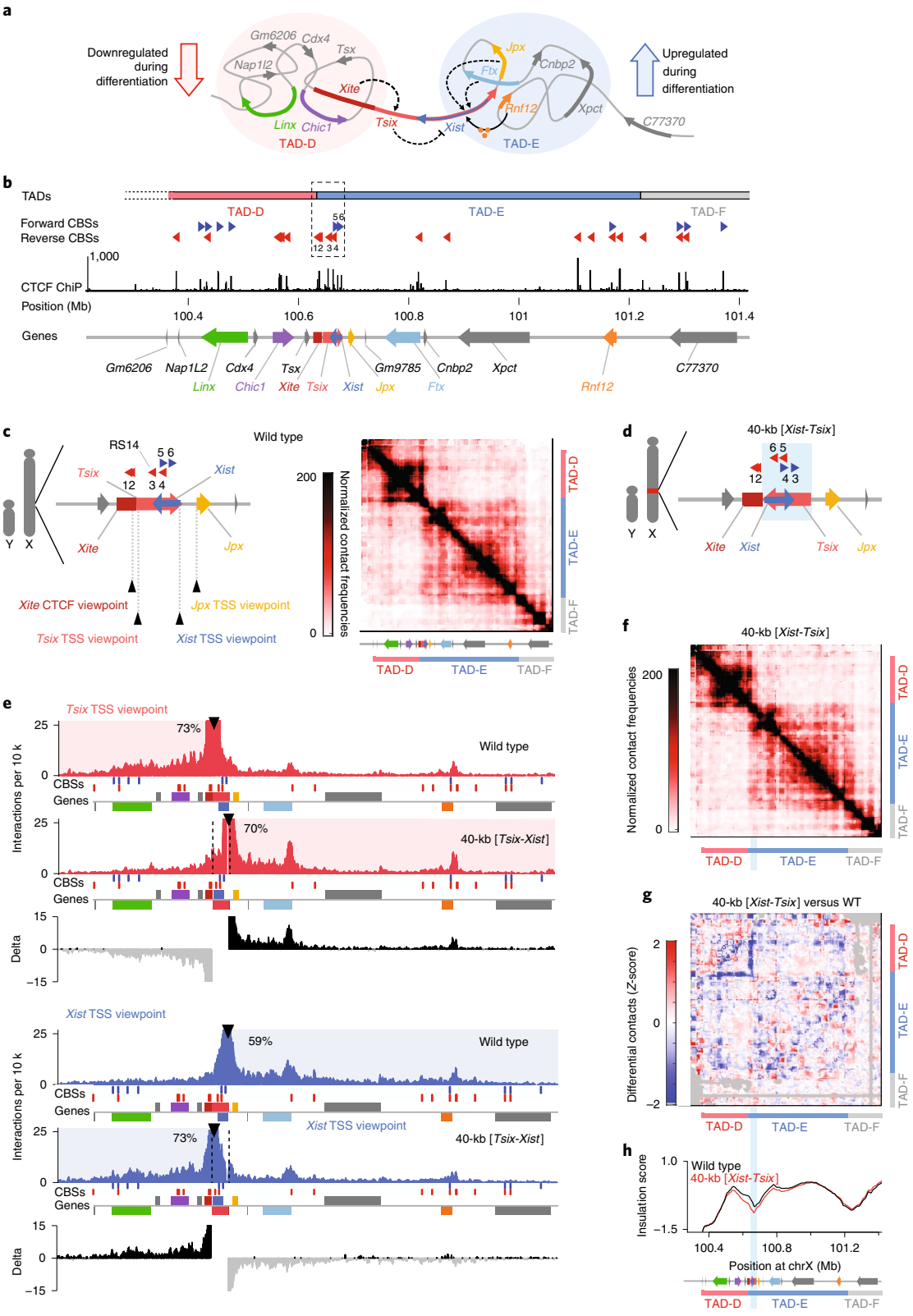

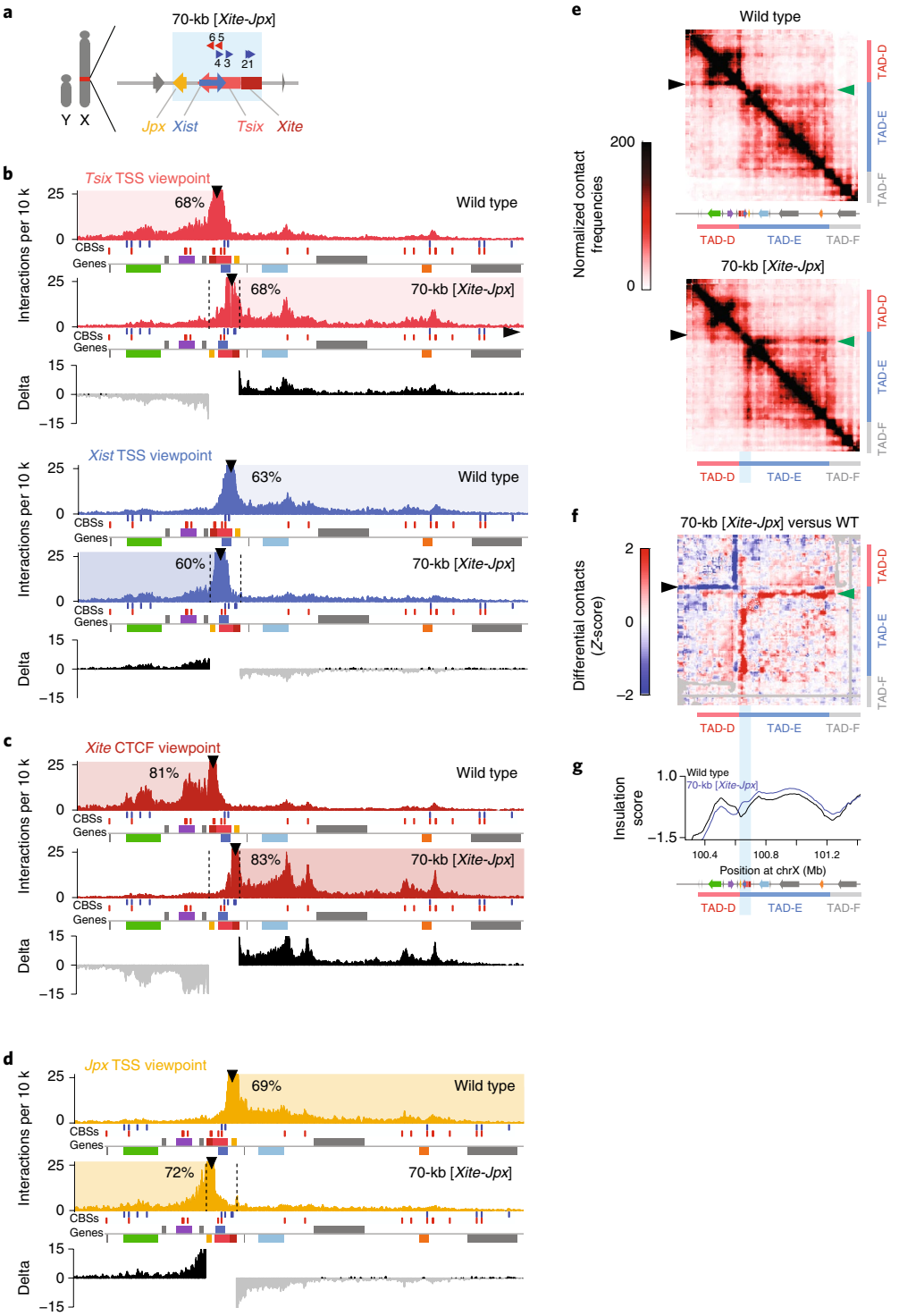

Fig. 2 | Genomic inversion of the *Xist/Tsix* loci along with *Xite* and *Jpx* leads to topological changes within the *Xic*. **a**, Schematic representation of the 70-kb [*Xite-Jpx*] inversion in male mESCs. Blue shaded box indicates inverted region. **b**, Capture-C profiles and differential interaction frequencies, as in Fig. 1e, for *Tsix* (red) and *Xist* (blue) viewpoints in wild type and 70-kb [*Xite-Jpx*] inversion. **c**, Capture-C profiles and differential interaction frequencies, as in Fig. 1e, for *Xite* (dark red) viewpoint in wild type and 70-kb [*Xite-Jpx*] inversion. **d**, Capture-C profiles and differential interaction frequencies, as in Fig. 1e, for *Jpx* (yellow) viewpoint in wild type and 70-kb [*Xite-Jpx*] inversion. **e**, 5C chromosome conformation contact frequencies in wild type male mESCs (top) or harboring a 70-kb [*Xite-Jpx*] inversion (bottom). Pool of two replicates each, data for inversion have been inverted accordingly (that is, the map represents the inverted genome), normalized and binned as in Fig. 1c. Arrowheads indicate interactions described in the text. **f**, Differential map represents the subtraction of wild type *Z*-scores from inversion *Z*-scores (see Methods). Gray pixels correspond to interactions that were filtered because they did not meet the quality control threshold (see Methods). Arrowheads indicate interactions described in the text. **g**, Insulation scores, wild type in black and 70-kb [*Xite-Jpx*] inversion in blue. Inverted region represented by light blue box. Chromosome positions are aligned with **e** and **f**. Note that each genomic alteration has been generated twice (two independent cell lines). Results for the first clone are shown here, results for the second clone are shown in Supplementary Figs. 2 and 3.

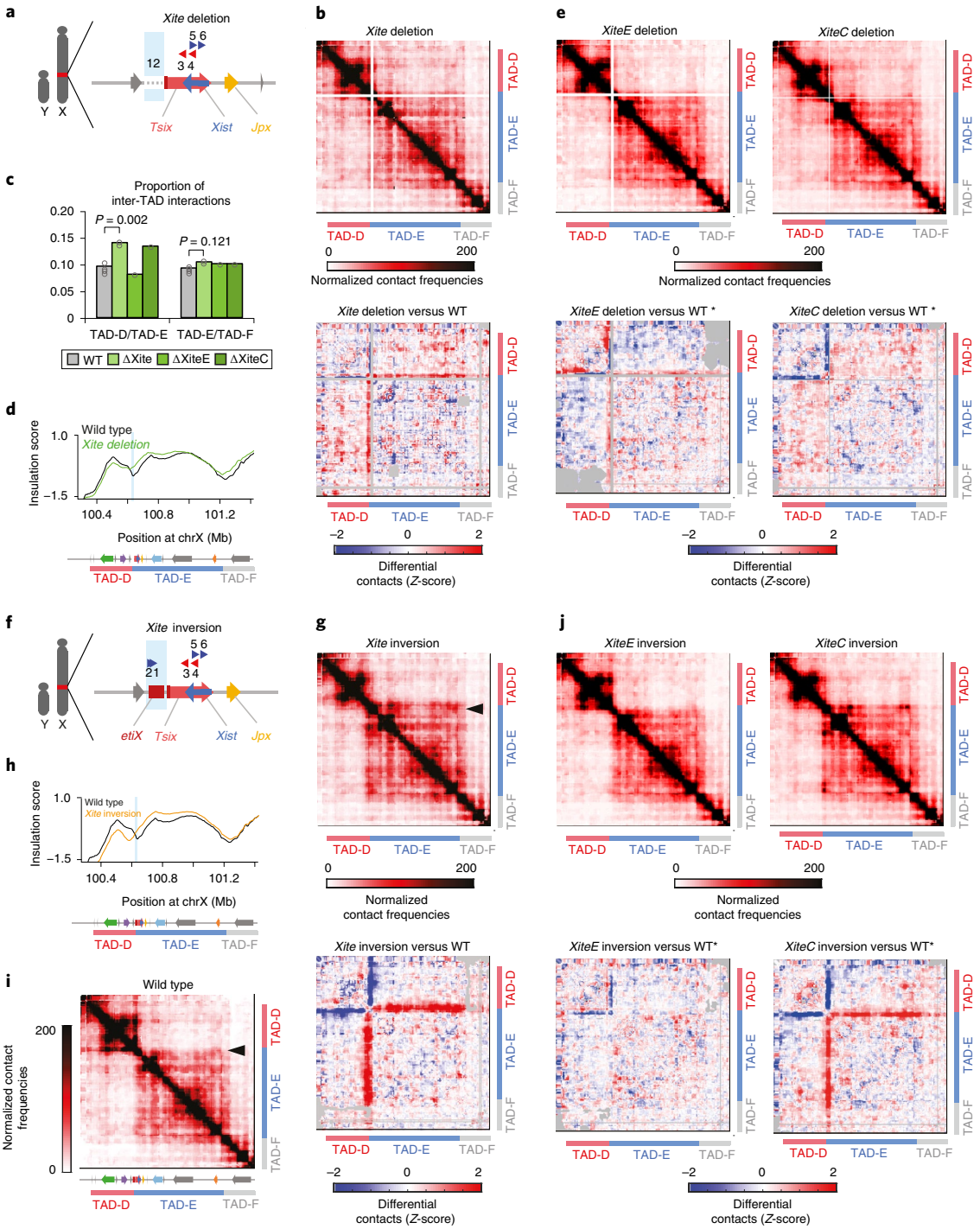

Fig. 3 | *Xite* structural element is important for TAD boundary position and insulation. a, Schematic representation of the *Xite* deletion (Δ*Xite*) in male mESCs. Blue box indicates deleted region. **b**,**e**,**g**,**j**, Top: 5C chromosome conformation contact frequencies in Δ*Xite* (**b**), Δ*XiteE* (**e**, left), Δ*XiteC* (**e**, right), *Xite* inversion (**g**), *XiteE* inversion (**j**, left) or *XiteC* inversion (**j**, right) male mESCs. Pools of two replicates normalized and binned as in 1C. Bottom: differential 5C map of mutant versus wild type mESCs. Differential map represents the subtraction of wild type *Z*-scores from mutant *Z*-scores (see Methods). Gray pixels correspond to interactions that were filtered because they did not meet the quality control threshold (see Methods). 5C results of Δ*Xite* and *Xite* inversion for the first clone shown here, second clone shown in Supplementary Fig. 3. For other mutants, maps represent pooled results from two independent clones. Asterisks in **e** and **j** denote that the wild type (WT) maps used for the differential analysis are not the same as in other figures; *XiteE* and *XiteC* mutants were processed as a different batch, which included its own wild type sample. **c**, Quantification of the increased inter-TAD interactions in *Xite* mutants. Center values represent the average of the calculated proportions: for ΔXiteE and ΔXiteC, two measurements each from two independent clones; for wild type and ΔXite, four measurements each from two independent clones in duplicates (see Supplementary Fig. 3f for details). Statistical analysis was performed using two-sample, two-tailed heteroscedastic *t*-test. **d**, Insulation scores; wild type in black and Δ*Xite* in green. Deleted region represented by light blue box. Insulation score for one clone shown here, second clone can be found in Supplementary Fig. 3e. **f**, Schematic representation of the *Xite* inversion in male mESCs. Blue box indicates inverted region. **h**, Insulation scores, wild type in black and *Xite* inversion in orange. Inverted region represented by the light blue box. Insulation score for one clone shown here, the second clone can be found in Supplementary Fig. 3e. **i**, 5C chromosome conformation contact frequencies in wild type male mESCs, as in Fig. 1c, included for clarity purposes. Arrowhead indicates interactions at the proximal end of TAD-E.

TAD-E in the inverted allele, confirming what we observed with the Capture-C for *Xite* (Fig. 2c and Supplementary Note 1). Thus the 70-kb inversion revealed similarities and differences compared to the 40-kb inversion. The promoters of *Xist* and *Tsix* switched interaction profiles in both cases, and the bipartite TAD structure was conserved. However, substantial changes occurred within the TADs in the 70-kb inversion, apparently associated with loss of *Xite* within TAD-D and its new position within TAD-E. Notably, compared to the 40-kb inversion, the 70-kb inversion displaced an extra pair of CBSs found within *Xite* (CBSs nos. 1–2); therefore, the final configuration of CBSs in the inverted allele is not equivalent to wild type (compare Fig. 1c to Fig. 2a). The structural phenotypes observed in the 70-kb inversion, where the orientation of the two *Xite* CBSs become convergent with those present within TAD-E, are consistent with recent models for CTCF-mediated loops, whereby CBSs in convergent orientation are more likely to interact with each other, forming the apex of cohesin-extruded loops[15–21].

***Xite* contributes to insulating the *Xist/Tsix* TADs and establishes a TAD boundary in an orientation-dependent manner.** The above results suggested that the CBSs within *Xite* have a strong influence on TAD structure and organization. To test this more directly, we generated deletions and inversions of the *Xite* locus (~18 kb) (Fig. 3a,f and Supplementary Fig. 1a). 5C analysis of the Δ*Xite* male mESCs (Fig. 3b for clone no. 1, and Supplementary Fig. 3c,d for clone no. 2) revealed a significant increase (45%) in contacts between TAD-D and TAD-E (Fig. 3c), suggesting that *Xite* is important for topological insulation between these TADs, also indicated by the insulation score profile (Fig. 3d and Supplementary Fig. 3e). The *Xite* locus includes an enhancer element (*XiteE*, ~12 kb)[44], and a structural element (*XiteC*, ~6 kb)[49] with two CBSs (CBSs nos. 1 and 2) in the same orientation. Transcription factor binding to enhancers as well as CBSs have been proposed to play roles in looping and long-range interactions. To distinguish between the contributions of the enhancer versus the structural element, *XiteE* and *XiteC* were each deleted alone (Supplementary Fig. 1). 5C analysis of Δ*XiteC* and Δ*XiteE* male mESCs (Fig. 3e) revealed an increase in contacts between TAD-D and TAD-E only in Δ*XiteC* mESCs (Fig. 3c), suggesting that it is the structural element within *Xite*, harboring two CBSs, that contributes to insulating TAD-D and TAD-E from each other (Supplementary Note 2).

We also investigated the topological consequences of inverting *Xite* (Fig. 3f). In *Xite*-inversion cells, we observed a localized gain of interactions between *Xite* (inverted) and sequences along TAD-E (Fig. 3g and Supplementary Figs. 3c–e and 4a), accompanied by a localized loss of structure in TAD-D. This suggests that inverting *Xite* switched its interacting preference from TAD-D to TAD-E, consistent with the new orientations of the two CBSs present within *Xite* (compare Fig. 3f to Fig. 1c). These results also support a role for *Xite* in the structural changes observed in the 70-kb inversion (Fig. 2e,f). The insulation score profile of the *Xite*-inversion allele revealed that the minimum value between the two TADs was shifted ~60 kb compared to wild type (Fig. 3h and Supplementary Fig. 3e). This indicates that the position of the TAD boundary has changed, as corroborated by an increase in size of TAD-E (compare arrowheads in Fig. 3g and i). To distinguish between the contributions of the enhancer versus the structural element in this altered architecture, we also generated inversions of *XiteE* and *XiteC* alone (Supplementary Fig. 1). Inversion of *XiteC*, but not of *XiteE*, led to similar changes to those observed with *Xite*-inversion (Fig. 3j and Supplementary Fig. 4a). On the basis of the analysis of this collection of *Xite* deletions and inversions, we conclude that the *Xite* structural element plays an important role in shaping the topological landscape of TAD-D and TAD-E and in promoting insulation between the two TADs.

The fact that loss of *Xite* did not result in a collapse or merging of the two TADs suggests that insulation between the TADs can be maintained by other elements (see Discussion for more details). Presumably, the numerous different CBSs present in both TAD-D and TAD-E, and at the boundary between them, can act redundantly to provide some degree of insulation between these TADs, even when the *Xite* structural element is removed. Deleting any of those CBSs alone may have little effect; indeed, we deleted CBS no. 3 (or RS14, ref. [50]), which was previously postulated to be a boundary element[50,51], and observed no loss of TAD insulation (Supplementary Fig. 5 and Supplementary Note 3).

***Xist* is aberrantly upregulated in male mESCs when placed in the regulatory landscape of *Tsix*.** We next addressed whether expression of *Xist* and *Tsix* was affected in the 40-kb and 70-kb inverted alleles, in which their respective promoters are exposed to each other's topological and regulatory environment (Figs. 1 and 2). We assessed the expression status of several genes, including those within the

Fig. 4 | *Xist/Tsix* inversions lead to ectopic *Xist* expression, Xist RNA coating and X-linked gene silencing in male mESCs. a, nCounter RNA expression levels in 40-kb inversion (red), 70-kb inversion (blue) and wild type (gray). Each inversion has its corresponding wild type comparison because they were processed in different batches. Bars depict the mean of two independent experiments, with dots depicting the independent experiments. **b**, Xist RNA accumulation analyzed by RNA–FISH in male wild type (gray), 40-kb inversion (red) and 70-kb inversion (blue) mESCs. Each inversion has its corresponding wild type comparison because they were processed in different batches. Bars represent mean percentage of counted cells with either a Xist pinpoint, Xist accumulation or full Xist cloud. Dots represent independent experiments. $n = 3$ independent experiments, each experiment counting 100–400 cells (Supplementary Table 6 for exact sample size details). Statistical analysis was performed on independent experiments, using a two-sided Fisher's exact test, mutant versus wild type. $^{*}P < 0.05$ in all three experiments, see Supplementary Table 8 for exact *P* values. Scale bar, 2 μm, images at same scale. **c**, Violin plots indicating Xist RAP enrichment at the X chromosome. Substantial and significant enrichment in the 40-kb inversion (red), and slight but significant enrichment in the 70-kb inversion (blue) compared to wild type (gray). The *x* axis depicts mean RAP signal normalized to input. $n = 2$ independent experiments). Box corresponds to 25th and 75th percentiles, black line to the median, whiskers to 1.5× the interquantile range (IQR) and dots to individual datapoints beyond the 1.5× IQR. Statistical analysis was performed using a two-sided Wilcoxon Rank Sum test. **d**, Xist RAP signal (normalized to input, mean of two replicates) along the entire X chromosome in wild type (gray), 40-kb [*Tsix-Xist*] inversion (red) and 70-kb [*Xite-Jpx*] inversion (blue) male mESCs, in comparison to Xist RAP signal in female mouse lymphatic fibroblasts (MLF) (dotted line). **e**, X-linked gene silencing represented by the mRNA expression ratio between X-linked genes and bootstrapped autosomal genes ($n = 1{,}000$). Box plots represent the median (black line), 25–75% (box), 1.5× IQR (whiskers) and outliers (dots) of the bootstrap ratios. Statistical analysis was performed using a two-sided Wilcoxon Rank Sum test. **f**, X-linked gene silencing specific for *Xist*-bound genes, as shown by the difference in $\log_2$ fold-change in mRNA expression levels between inversion and wild type cells, for genes not bound by Xist RNA (labeled as no Xist) versus genes that are bound by Xist RNA (labeled as Xist). Box plots represent the median (black line), 25–75% (box) and 1.5× IQR (whiskers). Genes were classified as bound by Xist RNA when RAP signal at the TSS > 7.5, n = number of genes in each group. Statistical analysis was performed using a two-sided Wilcoxon Rank Sum test. NS, not significant. **g**, Schematic illustration of the effects of inverting *Tsix-Xist* (40 kb) and *Xite-Jpx* (70 kb) on transcriptional activity in male mESCs. Note that each inversion has been generated in two independent cell lines. Results for the second clones are shown in Supplementary Fig. 6.

Xic, in wild type and mutant male mESCs. In both the 40-kb [*Tsix-Xist*] and the 70-kb [*Xite-Jpx*] inversions, expression of *Tsix* was not significantly affected, despite its new genomic location (Fig. 4a and Supplementary Fig. 6a for the second clone). On the other hand, *Xist* became significantly upregulated when placed within TAD-D: 38- and 18-fold in two independent 40-kb clones; 4- and 2.6-fold in two independent 70-kb clones (Fig. 4a and Supplementary Fig. 6a). Upregulation of *Xist* does not normally occur in male mESCs, presumably due to *Xist*-repressive mechanisms operating in mESCs (such as pluripotency and *Tsix*) and to the absence of a double dose of X-linked *Xist* activators. Relocation of the *Xist* promoter into TAD-D and its *cis*-regulatory environment in our inversions seems to override such mechanisms/requirements. In addition, transcriptional analysis in our collection of *Xite* inversions revealed that *Xist* expression is sensitive to the orientation of *Xite* structural element (*XiteC*) (see Supplementary Note 4 and Supplementary Fig. 4b–e). Taken together, our results highlight how critical the *cis*-regulatory landscape is for appropriate *Xist* regulation.

We also observed that, for the 40-kb [*Tsix-Xist*] inversion, *Cdx4* (in TAD-D) and *Ftx*, *Xpct* and *Rnf12* (in TAD-E) were all downregulated two-fold or more (red bars in Supplementary Fig. 6a). To address whether this could be due to ectopically expressed *Xist* RNA

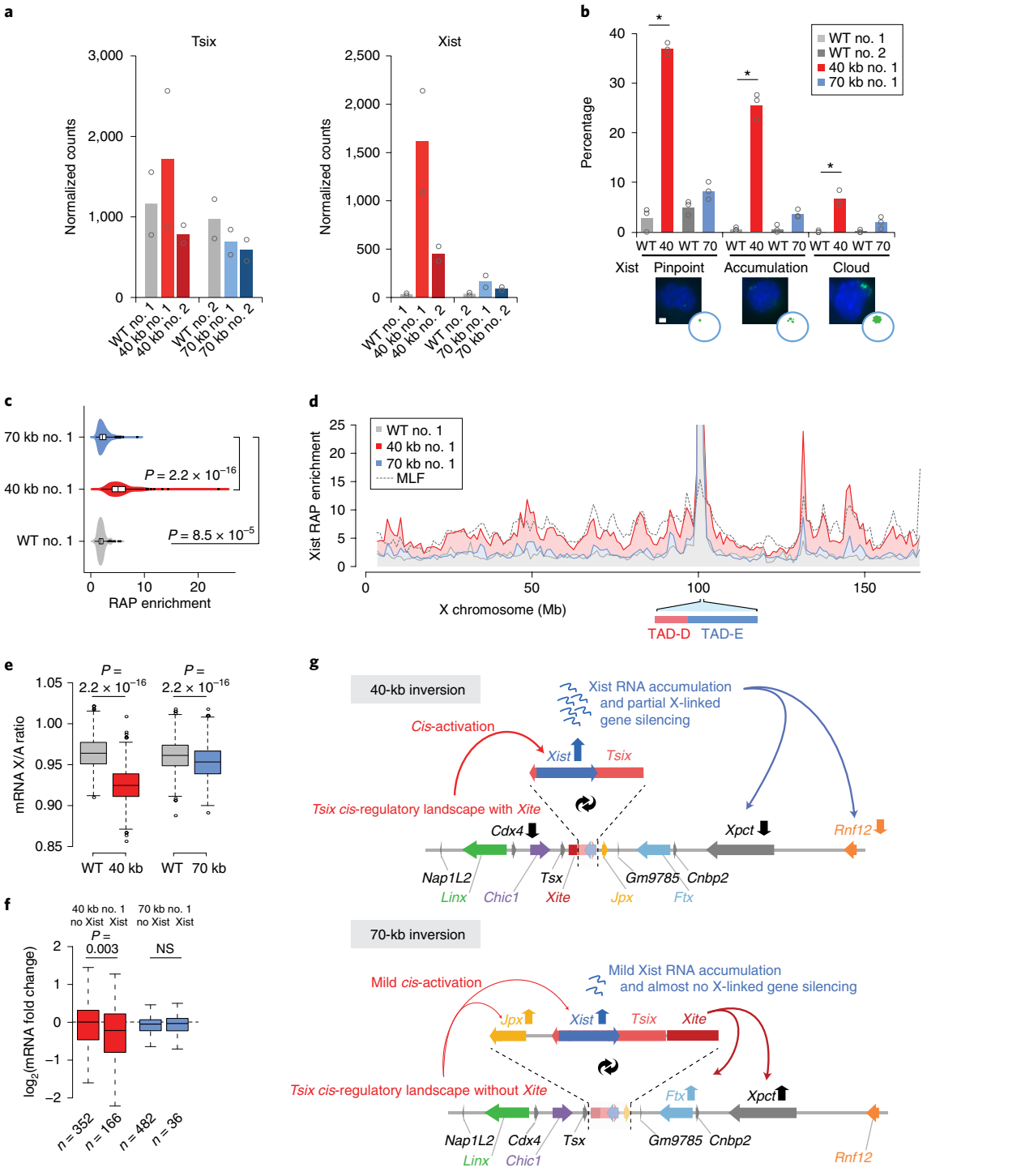

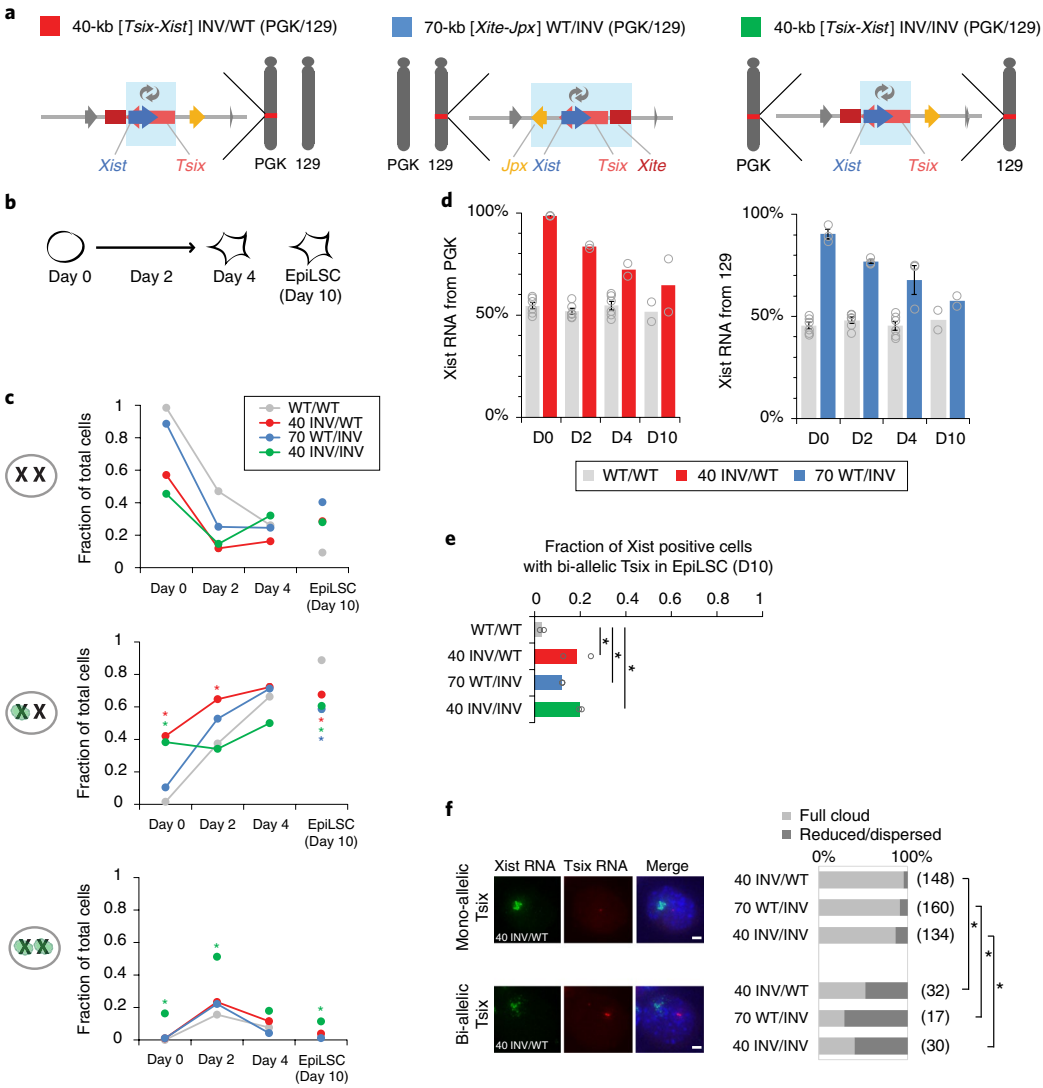

Fig. 5 | *Xist/Tsix* inversions affect the initiation of XCI and the expression dynamics of *Xist* and *Tsix* during differentiation of female mESCs. a, Schematic representation of female hybrid mESC lines harboring a heterozygous 40-kb [*Tsix-Xist*] inversion on the PGK chromosome (red), a 70-kb [*Xite-Jpx*] inversion on the 129 chromosome (blue) and a homozygous 40-kb [*Tsix-Xist*] inversion (green). Light blue boxes indicate inverted region. **b**, Schematic representation of mESC to EpiLSC differentiation and time points analyzed. **c**, Xist RNA accumulation analyzed by RNA–FISH in the female cell lines described in **a**. Bars represent mean fraction of counted cells with an Xist RNA accumulation or cloud at none, one and both X chromosomes. For each cell line, at least two independent experiments were performed, each counting >100 cells (Supplementary Table 6 for the number of independent experiments per cell line and exact sample size details). Statistical analysis was performed on independent experiments, using a two-sided Fisher's exact test, mutant versus wild type per time point. $^*P < 0.05$ in all experiments, see Supplementary Table 8 for exact *P* values. **d**, Allelic *Xist* expression, measured by pyrosequencing of *Xist* cDNA. Bars represent the percentage of Xist RNA expressed from the PGK (left) or 129 (right) allele in cells described in **a**. Bars depict the mean of two or more independent experiments, with dots depicting each experiment, and error bars representing s.e.m. in case of $n > 3$ (number of independent experiments per line as in **c**). **e**, Bi-allelic *Tsix* expression measured by RNA–FISH in the female cell lines described in **a**. Bars represent mean fraction of Xist-positive cells with bi-allelic *Tsix* expression. For each cell line, two independent experiments were performed, each counting >100 cells (see Supplementary Table 6 for exact sample size details). Dots represent the independent experiments. Statistical analysis was performed on independent experiments, using Pearson's chi-squared test with Yates' continuity correction: $^*P \leq 0.01$ in both experiments. See Supplementary Table 8 for exact *P* values. **f**, Quantification of Xist RNA cloud formation in the female cell lines described in **a**, at day 10 of EpiLSC induction. Typical example of a proper Xist RNA cloud in a 40 INV/WT cell that expresses Tsix RNA from one X chromosome (upper panels). Typical example of a reduced and dispersed Xist RNA cloud formation in a 40 INV/WT cell that expresses Tsix RNA from both X chromosomes (lower panels). Bar plot shows mean percentages of cells with full Xist RNA cloud formation (light gray) and reduced/dispersed Xist RNA cloud formation (dark gray) in Xist-positive cells expressing Tsix RNA from one or neither of the X chromosomes (top bars) or cells expressing Tsix RNA from both X chromosomes (bottom bars). $n = 2$ independent experiments, total number of cells in the two experiments per group noted between brackets. Statistical analysis was performed on each independent experiment using a two-sided Fisher's exact test. $^*P < 0.01$ in both experiments. See Supplementary Table 8 for exact *P* values.

leading to some degree of gene silencing, we performed RNA–fluorescence in situ hybridization (FISH), RNA antisense purification (RAP) and messenger RNA sequencing on our male mutants and controls. *Xist* expression is mostly absent in wild type male mESCs as measured by RNA–FISH (<6% of cells); however, in cells harboring the 40-kb [*Tsix-Xist*] inversion, we observed that ~70/40% of

cells expressed *Xist* (in the two clones, respectively), with a significant percentage of cells (~30/13%) exhibiting Xist RNA accumulation or even larger cloud formation (red bars in Fig. 4b for clone no. 1 and Supplementary Fig. 6c for clone no. 2). Concomitantly, we observed significant Xist RNA coating of the X chromosome by RAP (Fig. 4c,d, in red), following a pattern similar to the Xist-coated inactive X in mouse fibroblasts[52] (dotted line Fig. 4d, $r=0.75$). In the 70-kb [*Xite-Jpx*] inversion, Xist RNA showed abnormal accumulation by RNA–FISH in 9–14% of cells (blue bars in Fig. 4b for clone no. 1 and Supplementary Fig. 6c for clone no. 2), but no substantial X-chromosome coating by RAP (Fig. 4c,d, in blue). This is consistent with the lesser degree of *Xist* upregulation observed in the 70-kb inversion compared to the 40-kb inversion (Fig. 4a and Supplementary Fig. 6a). Finally, we determined mRNA transcription levels of autosomal and X-linked genes by RNA-seq. RNA-seq analyses confirmed the changes in gene expression within the *Xic* described above (Supplementary Fig. 6b). For a chromosome-wide analysis of X-linked silencing, we calculated X/autosome (X/A) expression ratios as a measure of dosage compensation[53]; in wild type male mESCs, this ratio was 0.97 (Fig. 4e). The X/A ratio in the two 40-kb (*Tsix-Xist*) clones decreased mildly but significantly to 0.91 and 0.92 (Wilcoxon rank sum test, $P \leq 2.2\times10^{-16}$) (Fig. 4e and Supplementary Fig. 6d, in red). This mild silencing was specific to genes enriched for Xist RNA at their TSS (Fig. 4f, in red). Limited X-linked gene silencing was significant in one 70-kb [*Xite-Jpx*] inversion clone but not in the other (Fig. 4e and Supplementary Fig. 6d, in blue), consistent with the other results.

Taken together, our results show that relocating the *Xist* promoter from TAD-E into TAD-D, with or without its local regulator *Jpx*, leads to ectopic *Xist* activation in male mESCs (summarized in Fig. 4g, see Supplementary Note 5). This underlines the importance of the TAD environment for the appropriate transcriptional regulation of *Xist*. It also highlights the relevance of the spatial partitioning between TAD-D and TAD-E and their *cis*-regulatory landscapes, as the *Xist/Tsix* TAD boundary seems to physically insulate the *Xist* promoter from the activating influence of elements within the *Tsix* TAD.

Perturbed initiation of XCI when inverting the genomic organization of *Xist* and *Tsix*. To investigate the consequences of our genomic inversions on the regulation of *Xist* and *Tsix* during X-inactivation, we generated the 40-kb and 70-kb inversions in female mESCs with polymorphic X chromosomes (PGK12.1-derived, see Methods). We obtained a heterozygous 40-kb [*Tsix-Xist*] inversion (40-kb INV/WT), a heterozygous 70-kb [*Xite-Jpx*] inversion (70-kb WT/INV) and a homozygous 40-kb [*Tsix-Xist*] inversion (40-kb INV/INV) (Fig. 5a). To trigger XCI, we differentiated wild type and mutant female mESCs toward epiblast-like stem cells (EpiLSCs)[54,55] (see Methods and Fig. 5b) and analyzed the kinetics of Xist RNA accumulation using RNA–FISH at days 0, 2 and 4. We also analyzed day 10 EpiLSCs that were independently generated; at this stage, in most cells, *Xist* is expressed from the inactive X, whereas *Tsix* is repressed on the inactive X and has also started to be silenced on the active X. In undifferentiated mESCs harboring the heterozygous or homozygous 40-kb [*Tsix-Xist*] inversion, we observed abnormal Xist RNA accumulation in ~40 or ~55% of the cells, respectively (Fig. 5c, second and third panel, day 0); 16% of homozygous-inversion cells showed ectopic Xist RNA accumulation on both chromosomes. In female mESCs harboring the heterozygous 70-kb [*Xist-Jpx*] inversion, ectopic Xist RNA accumulation was also observed, although in fewer cells (~10%) (Fig. 5c, second panel, day 0). Allelic quantification of Xist RNA by pyrosequencing confirmed that the ectopic Xist RNA accumulation originated from the inverted allele in both 40- and 70-kb inversions (Fig. 5d, day 0). These results demonstrate that in female mESCs, similarly to male mESCs, *Xist trans*-repression mechanisms operating in mESCs are not sufficient to prevent *cis*-activation of the *Xist* promoter when it is placed within *Tsix*'s regulatory landscape.

During differentiation, the initial differences between wild type and mutant cells decreased over time (Fig. 5c, days 2 and 4); at day 4, the proportion of cells accumulating Xist RNA on one or two X chromosomes was equivalent across all cell lines (~70%) (Fig. 5c, day 4). Furthermore, in day 10 EpiLSCs cells harboring an inversion, the percentage of cells with accumulation of *Xist* was significantly reduced to ~60%, compared to ~90% in wild type (Fig. 5c, day 10). Notably, all cell lines harboring inversions exhibited normal differentiation hallmarks (Supplementary Fig. 7c,d) and did not suffer X-chromosome loss. In addition, pyrosequencing confirmed that throughout differentiation the fraction of Xist RNA from the inverted allele decreased significantly over time (Fig. 5d). This suggests that *Xist* expression and/or accumulation is impaired during differentiation of female mESC harboring the inversions (see also Supplementary Notes 6 and 7).

***Tsix* silencing is impaired when its promoter is exposed to *Xist*'s regulatory landscape.** We then evaluated *Tsix* nascent transcription by RNA–FISH in day 10 EpiLSCs harboring the 40-kb and 70-kb inversions. During differentiation of wild type female mESCs, *Tsix* transcription becomes rapidly repressed on the chromosome that expresses *Xist*[31–33]. This transition from bi-allelic to mono-allelic *Tsix* expression is almost complete in day 10 wild type EpiLSCs, with less than 5% of cells with a Xist RNA accumulation showing *Tsix* expression from both X chromosomes (Fig. 5e, gray bars). In both inversions, we found that global *Tsix* levels were increased (Supplementary Fig. 7g) and observed a significantly increased proportion of *Xist*-positive cells that expressed *Tsix* from the two X chromosomes (~10–20% chi-squared test, $P \leq 0.001$) (Fig. 5e). We conclude that exposing *Tsix* to the regulatory environment that normally belongs to *Xist* impairs *Tsix* silencing during differentiation, and leads to the co-occurrence of Xist RNA accumulation and *Tsix* expression from the same allele.

We also assessed whether Xist RNA clouds were affected in those cells in which *Xist* expression co-occurred with bi-allelic *Tsix* expression. We selected Xist-positive cells, and compared the Xist clouds in cells with bi-allelic *Tsix* expression to cells with no or mono-allelic *Tsix* expression (Fig. 5f). In cells that express *Tsix* from one or neither of the X chromosomes, we observed typical Xist RNA cloud formation in most cells (86–95%). In cells that express *Tsix* from both X chromosomes, this proportion was significantly reduced (29–52%) and a significant proportion of these cells (48–71%) showed a reduced or dispersed Xist RNA accumulation. Despite a low total number of cells with prolonged bi-allelic *Tsix* expression, the correlation between bi-allelic *Tsix* expression and reduced/dispersed Xist RNA clouds is highly significant (Fig. 5f). These results suggest that prolonged *Tsix* expression might contribute to the reduced levels of Xist RNA during differentiation in the inversions (see also Supplementary Note 6).

Taken together, our results indicate that the original configuration prevents the *Xist* and *Tsix* promoters from frequently interacting with each other's regulatory environment, and that this is critical for appropriate *Xist* expression and timely *Tsix* repression during differentiation. We propose that the partitioning into two TADs ensures correct XCI by insulating *Xist* and *Tsix* regulatory environments from each other.

Discussion

In this study, we addressed the extent to which topological and regulatory environments are critical for the appropriate developmental regulation of *Xist* and *Tsix*. We found that the promoters of *Xist* and *Tsix*, when relocated into each other's TAD, lost their original chromosomal interactions to some extent and adopted novel interactions mostly restricted to, and guided by, the new TAD within

which they lay, consistent with similar findings at other loci in the genome[16,56,57]. This allowed us to specifically address the functional impact of switching the TAD environment of two promoters at once.

The *Tsix* and *Xist* promoters exhibited different behaviors when moved to a new TAD environment. While *Tsix* steady-state expression levels seemed unaffected in mESCs (discussed below), we observed aberrant activation of *Xist* on relocation of its promoter to TAD-D. This led to Xist RNA accumulation, X chromosome coating and partial gene silencing (Fig. 4). This ectopic upregulation of *Xist* could be due to the loss of its native *cis*-regulatory landscape and/or gain of a new environment. Given that a deletion spanning most of *Xist* TAD, from *Jpx* up to *Rnf12*, did not lead to aberrant upregulation of *Xist* expression[46], we favor the second hypothesis: exposure to TAD-D and the *cis*-regulatory environment of *Tsix*, which is normally active in mESCs[3], led to *Xist* upregulation. This ectopic upregulation is milder in the 70-kb inversion than in the 40-kb inversion probably because the TAD-D landscape is a less potent 'activator' without *Xite*.

In contrast, *Tsix* expression in male mESCs seems unchanged when its promoter is placed in the *Xist* TAD (Fig. 4), suggesting that *Tsix* is much less sensitive to its *cis*-regulatory environment in the pluripotent state (see also Supplementary Note 8). However, during female differentiation, we showed that displacing the promoter of *Tsix* into the *Xist* TAD led to co-occurrence of *Tsix* expression and Xist RNA accumulation on the same allele (Fig. 5). This abnormal *Tsix* expression is probably sustained or reignited by the *cis*-regulatory environment of TAD-E, in which other loci are normally able to 'escape' Xist-mediated silencing (for example, *Jpx, Ftx*)[58,59]. Taken together, our results highlight how the sensitivity of a promoter to its *cis*-environment can depend on distinct cell states, and that in some instances the *cis*-regulatory environment can have a dominant effect over *trans*-acting mechanisms.

Our study also provides important insights into the *Xist*/*Tsix* TAD boundary, a rather typical TAD boundary on the X chromosome in terms of its insulation strength (Supplementary Fig. 3g). Inversion of the 40-kb region led to a switch in the *Xist* and *Tsix* interaction profiles, which suggests that elements in the inverted region are able to restrict and direct the interactions of the *Xist* and *Tsix* promoters. Moreover, we identified *Xite* as a critical element for TAD boundary position and insulation (Fig. 3). *Xite* not only lies very close to the *Xist*/*Tsix* boundary but also harbors a pair of CBSs that mediate strong intra-TAD interactions. Our data thus provide support for previous proposals that the interactions within TADs can contribute to defining TAD boundaries, by preventing interactions with neighboring TADs and creating a boundary by default[49,60]. The formation of the *Xist* and *Tsix* TADs probably arises from a combination of both intra-TAD scaffolding, and insulator elements.

In summary, the appropriate kinetics and allelic regulation of *Xist* and *Tsix* during XCI require *Xic*'s *cis*-regulatory landscape, but also its spatial partitioning, which prevents exposure of *Xist* to the *cis*-regulatory elements within the *Tsix* TAD and vice versa. Identifying the exact sequences responsible for this bipartite TAD structure (and its boundary), as well as all the sequences that regulate *Xist* and *Tsix* in a TAD-specific manner, are interesting avenues of future research. In light of our results, we propose that the spatial partitioning of the *Xic* is an integral part of its definition as the minimal locus necessary and sufficient to trigger XCI[22–25]. The two *Xic* TADs serve to (1) insulate *Xist* physically from frequent *cis*-regulatory influences of the *Tsix* TAD in embryonic stem cells (ESCs), (2) provide the required *cis*-regulatory landscape for *Xist* to be upregulated during differentiation and (3) shield *Tsix* from the regulatory influences exerted by the *Xist* TAD during early differentiation. Our study further validates the *Xic* as a genetic model to understand how three-dimensional genome organization can affect the regulation of transcriptional dynamics during developmental processes.

Online content

Any methods, additional references, Nature Research reporting summaries, source data, statements of code and data availability and associated accession codes are available at https://doi.org/10.1038/s41588-019-0412-0.

Received: 4 March 2018; Accepted: 4 April 2019;
Published online: 27 May 2019

References

1. de Laat, W. & Duboule, D. Topology of mammalian developmental enhancers and their regulatory landscapes. *Nature* **502**, 499–506 (2013).
2. Dixon, J. R. et al. Topological domains in mammalian genomes identified by analysis of chromatin interactions. *Nature* **485**, 376–380 (2012).
3. Nora, E. P. et al. Spatial partitioning of the regulatory landscape of the X-inactivation centre. *Nature* **485**, 381–385 (2012).
4. Phillips-Cremins, J. E. et al. Architectural protein subclasses shape 3D organization of genomes during lineage commitment. *Cell* **153**, 1281–1295 (2013).
5. Rao, S. S. et al. A 3D map of the human genome at kilobase resolution reveals principles of chromatin looping. *Cell* **159**, 1665–1680 (2014).
6. Zhan, Y. et al. Reciprocal insulation analysis of Hi-C data shows that TADs represent a functionally but not structurally privileged scale in the hierarchical folding of chromosomes. *Genome Res.* **27**, 479–490 (2017).
7. Vietri Rudan, M. et al. Comparative Hi-C reveals that CTCF underlies evolution of chromosomal domain architecture. *Cell Rep.* **10**, 1297–1309 (2015).
8. Le Dily, F. et al. Distinct structural transitions of chromatin topological domains correlate with coordinated hormone-induced gene regulation. *Genes Dev.* **28**, 2151–2162 (2014).
9. Shen, Y. et al. A map of the cis-regulatory sequences in the mouse genome. *Nature* **488**, 116–120 (2012).
10. Symmons, O. et al. Functional and topological characteristics of mammalian regulatory domains. *Genome Res.* **24**, 390–400 (2014).
11. Van Bortle, K. et al. Insulator function and topological domain border strength scale with architectural protein occupancy. *Genome Biol.* **15**, R82 (2014).
12. Li, Y. et al. Characterization of constitutive CTCF/cohesin loci: a possible role in establishing topological domains in mammalian genomes. *BMC Genomics* **14**, 553 (2013).
13. Sofueva, S. et al. Cohesin-mediated interactions organize chromosomal domain architecture. *EMBO J.* **32**, 3119–3129 (2013).
14. Nora, E. P. et al. Targeted degradation of CTCF decouples local insulation of chromosome domains from genomic compartmentalization. *Cell* **169**, 930–944 e22 (2017).
15. Guo, Y. et al. CRISPR inversion of CTCF sites alters genome topology and enhancer/promoter function. *Cell* **162**, 900–910 (2015).
16. Lupianez, D. G. et al. Disruptions of topological chromatin domains cause pathogenic rewiring of gene-enhancer interactions. *Cell* **161**, 1012–1025 (2015).
17. Sanborn, A. L. et al. Chromatin extrusion explains key features of loop and domain formation in wild-type and engineered genomes. *Proc. Natl Acad. Sci. USA* **112**, E6456–E6465 (2015).
18. de Wit, E. et al. CTCF binding polarity determines chromatin looping. *Mol. Cell* **60**, 676–684 (2015).
19. Narendra, V. et al. CTCF establishes discrete functional chromatin domains at the Hox clusters during differentiation. *Science* **347**, 1017–1021 (2015).
20. Tang, Z. et al. CTCF-mediated human 3D genome architecture reveals chromatin topology for transcription. *Cell* **163**, 1611–1627 (2015).
21. Lupianez, D. G., Spielmann, M. & Mundlos, S. Breaking TADs: how alterations of chromatin domains result in disease. *Trends Genet.* **32**, 225–237 (2016).
22. Rastan, S. Non-random X-chromosome inactivation in mouse X-autosome translocation embryos–location of the inactivation centre. *J. Embryol. Exp. Morphol.* **78**, 1–22 (1983).
23. Rastan, S. & Robertson, E. J. X-chromosome deletions in embryo-derived (EK) cell lines associated with lack of X-chromosome inactivation. *J. Embryol. Exp. Morphol.* **90**, 379–388 (1985).
24. Heard, E., Avner, P. & Rothstein, R. Creation of a deletion series of mouse YACs covering a 500 kb region around Xist. *Nucleic Acids Res.* **22**, 1830–1837 (1994).
25. Lee, J. T., Strauss, W. M., Dausman, J. A. & Jaenisch, R. A 450 kb transgene displays properties of the mammalian X-inactivation center. *Cell* **86**, 83–94 (1996).
26. Galupa, R. & Heard, E. X-chromosome inactivation: new insights into cis and trans regulation. *Curr. Opin. Genet. Dev.* **31**, 57–66 (2015).
27. Nesterova, T. B. et al. Pluripotency factor binding and Tsix expression act synergistically to repress Xist in undifferentiated embryonic stem cells. *Epigenetics Chromatin* **4**, 17 (2011).

28. Navarro, P. et al. Molecular coupling of Xist regulation and pluripotency. *Science* **321**, 1693–1695 (2008).
29. Sousa, E. J. et al. Exit from naive pluripotency induces a transient X chromosome Inactivation-like state in males. *Cell Stem Cell* **22**, 919–928 e6 (2018).
30. Lee, J. T. Regulation of X-chromosome counting by Tsix and Xite sequences. *Science* **309**, 768–771 (2005).
31. Debrand, E., Chureau, C., Arnaud, D., Avner, P. & Heard, E. Functional analysis of the DXPas34 locus, a 3′ regulator of Xist expression. *Mol. Cell Biol.* **19**, 8513–8525 (1999).
32. Lee, J. T., Davidow, L. S. & Warshawsky, D. Tsix, a gene antisense to Xist at the X-inactivation centre. *Nat. Genet.* **21**, 400–404 (1999).
33. Mise, N., Goto, Y., Nakajima, N. & Takagi, N. Molecular cloning of antisense transcripts of the mouse Xist gene. *Biochem. Biophys. Res. Commun.* **258**, 537–541 (1999).
34. Tian, D., Sun, S. & Lee, J. T. The long noncoding RNA, Jpx, is a molecular switch for X chromosome inactivation. *Cell* **143**, 390–403 (2010).
35. Barakat, T. S. et al. RNF12 activates Xist and is essential for X chromosome inactivation. *PLoS Genet.* **7**, e1002001 (2011).
36. Furlan, G. et al. The Ftx noncoding locus controls X chromosome inactivation independently of its RNA products. *Mol. Cell* **70**, 462–472 e8 (2018).
37. Augui, S., Nora, E. P. & Heard, E. Regulation of X-chromosome inactivation by the X-inactivation centre. *Nat. Rev. Genet.* **12**, 429–442 (2011).
38. Pollex, T. & Heard, E. Recent advances in X-chromosome inactivation research. *Curr. Opin. Cell Biol.* **24**, 825–832 (2012).
39. van Bemmel, J. G., Mira-Bontenbal, H. & Gribnau, J. *Cis*- and *trans*-regulation in X inactivation. *Chromosoma* **125**, 41–50 (2016).
40. Hughes, J. R. et al. Analysis of hundreds of cis-regulatory landscapes at high resolution in a single, high-throughput experiment. *Nat. Genet.* **46**, 205–212 (2014).
41. Davies, J. O. et al. Multiplexed analysis of chromosome conformation at vastly improved sensitivity. *Nat. Methods* **13**, 74–80 (2016).
42. Dostie, J. et al. Chromosome conformation capture carbon copy (5C): a massively parallel solution for mapping interactions between genomic elements. *Genome Res.* **16**, 1299–1309 (2006).
43. Merkenschlager, M. & Nora, E. P. CTCF and cohesin in genome folding and transcriptional gene regulation. *Annu. Rev. Genom. Hum. Genet.* **17**, 17–43 (2016).
44. Ogawa, Y. & Lee, J. T. Xite, X-inactivation intergenic transcription elements that regulate the probability of choice. *Mol. Cell* **11**, 731–743 (2003).
45. Stavropoulos, N., Rowntree, R. K. & Lee, J. T. Identification of developmentally specific enhancers for Tsix in the regulation of X chromosome inactivation. *Mol. Cell Biol.* **25**, 2757–2769 (2005).
46. Barakat, T. S. et al. The trans-activator RNF12 and cis-acting elements effectuate X chromosome inactivation independent of X-pairing. *Mol. Cell* **53**, 965–978 (2014).
47. Sun, S. et al. Jpx RNA activates Xist by evicting CTCF. *Cell* **153**, 1537–1551 (2013).
48. Carmona, S., Lin, B., Chou, T., Arroyo, K. & Sun, S. LncRNA Jpx induces Xist expression in mice using both *trans* and *cis* mechanisms. *PLoS Genet.* **14**, e1007378 (2018).
49. Giorgetti, L. et al. Predictive polymer modeling reveals coupled fluctuations in chromosome conformation and transcription. *Cell* **157**, 950–963 (2014).
50. Spencer, R. J. et al. A boundary element between Tsix and Xist binds the chromatin insulator Ctcf and contributes to initiation of X-chromosome inactivation. *Genetics* **189**, 441–454 (2011).
51. Jegu, T., Aeby, E. & Lee, J. T. The X chromosome in space. *Nat. Rev. Genet.* **18**, 377–389 (2017).
52. Engreitz, J. M. et al. The Xist lncRNA exploits three-dimensional genome architecture to spread across the X chromosome. *Science* **341**, 1237973 (2013).
53. Brockdorff, N. & Turner, B. M. Dosage compensation in mammals. *Cold Spring Harb. Perspect. Biol.* **7**, a019406 (2015).
54. Brons, I. G. et al. Derivation of pluripotent epiblast stem cells from mammalian embryos. *Nature* **448**, 191–195 (2007).
55. Guo, G. et al. Klf4 reverts developmentally programmed restriction of ground state pluripotency. *Development* **136**, 1063–1069 (2009).
56. Franke, M. et al. Formation of new chromatin domains determines pathogenicity of genomic duplications. *Nature* **538**, 265–269 (2016).
57. Rodriguez-Carballo, E. et al. The HoxD cluster is a dynamic and resilient TAD boundary controlling the segregation of antagonistic regulatory landscapes. *Genes Dev.* **31**, 2264–2281 (2017).
58. Johnston, C. M., Newall, A. E., Brockdorff, N. & Nesterova, T. B. Enox, a novel gene that maps 10 kb upstream of Xist and partially escapes X inactivation. *Genomics* **80**, 236–244 (2002).
59. Chureau, C. et al. Ftx is a non-coding RNA which affects Xist expression and chromatin structure within the X-inactivation center region. *Hum. Mol. Genet.* **20**, 705–718 (2011).
60. Hofmann, A. & Heermann, D. W. The role of loops on the order of eukaryotes and prokaryotes. *FEBS Lett.* **589**, 2958–2965 (2015).
61. Kent, W. J. et al. The human genome browser at UCSC. *Genome Res* **12**, 996–1006 (2002).

Acknowledgements

We would like to thank the Heard laboratory for their technical input and critical discussions; D. Noordermeer for critical discussion and advice on Capture-C data analysis and interpretation; A. Chow from the Guttman laboratory for RAP-DNA cell culture; members of the Bourc'his laboratory; C. Reyes and A. Rapinat from the Nanostring platform and J. M. Telenius, M. Oudelaar and D. Downes from the Hughes and Higgs laboratories. This work was supported by an ERC Advanced Investigator award (ERC-2014-AdG no. 671027), Labelisation La Ligue, FRM (grant no. DEI20151234398), ANR DoseX 2017, Labex DEEP (no. ANR-11-LBX-0044), part of the IDEX Idex PSL (no. ANR-10-IDEX-0001-02 PSL) and ABS4NGS (no. ANR-11-BINF-0001) to E.H.; NWO-ALW Rubicon (no. 825.13.002) and Veni (no. 863.15.016) fellowships to J.G.v.B.; Région Ile-de-France (DIM Biothérapies) and Fondation pour la Recherche Médicale (no. FDT20160435295) fellowships to R.G.; Sir Henry Wellcome Postdoctoral Fellowship (no. 201369/Z/16/Z) to J.J.Z.; MRC Clinician Scientist Fellowship (no. MR/R008108) to J.D.; Wellcome Trust Strategic Award (no. 106130/Z/14/Z) to J.R.H.; New York Stem Cell Foundation and California Institute of Technology funds to M.G. (M.G. is a New York Stem Cell Foundation—Robertson Investigator); Novartis Foundation and European Research Council (ERC) under the European Union's Horizon 2020 research and innovation programme (grant agreement no. 759366 'BioMeTre') to L.G.; LabEx and EquipEx (nos. ANR-10-IDEX-0001-02 PSL, ANR-11-LBX-0044 and 'INCa-DGOS-4654' SIRIC11-002) to the Nanostring platform of Institut Curie; Equipex (no. ANR-10-EQPX-03), France Génomique Consortium from the Agence Nationale de la Recherche ('Investissements d'Avenir' program; no. ANR-10-INBS-09-08) and Cancéropole Ile-de-France and by the SiRIC-Curie program—SiRIC grant (no. INCa-DGOS-4654) to the ICGex Next Generation Sequencing platform of the Institut Curie.

Author contributions

J.G.v.B., J.G. and E.H. conceived the study, with support from R.G., L.G. and E.P.N. J.G.v.B., N.S. (lead), R.G., A.J.S., Y.Z., E.d.W. and L.G. (equal) conducted the formal analysis. J.G.v.B and R.G. led the investigation. C.G., A.J.S., C.P., E.P.N., J.J.Z. and S.L. supported the investigation. J.D., Y.Z., L.G., J.D., J.R.H. and D.R.H. provided resources. J.G.v.B. and E.H. wrote and prepared the original draft, with support from E.P.N., R.G. and C.G and input from all authors. R.G. and E.H. led the revision and editing of the article, with support from J.G.v.B. J.G.v.B. and R.G. provided data visualization. J.G.v.B., R.G. and E.H. supervised the study, with support from J.D., D.G., S.B., M.G., J.R.H., D.R.H. and J.G. The funding was acquired by E.H., J.G.v.B. and J.G.

Competing interests

The authors declare no competing interests.

Additional information

Supplementary information is available for this paper at https://doi.org/10.1038/s41588-019-0412-0.

Reprints and permissions information is available at www.nature.com/reprints.

Correspondence and requests for materials should be addressed to J.G.v.B. or E.H.

Publisher's note: Springer Nature remains neutral with regard to jurisdictional claims in published maps and institutional affiliations.

Methods

Design of inversions. The 40-kb [*Tsix-Xist*] inversion starts 315 base pairs (bp) upstream of the *Tsix* TSS, including the major *Tsix* promoter[45], the H3K27ac, H3K4me3, DNase I and p300 enriched region and the minisatellite region DxPas34, which is characterized as a component of the enhancer of *Tsix*[45]. The 40-kb [*Tsix-Xist*] inversion ends ~2 kb upstream of *Xist*, including the *Xist* promoter[62], which is enriched in H3K27ac and corresponds to a DNase I hypersensitive site (Supplementary Fig. 1a). The 70-kb [*Xite-Jpx*] inversion starts ~23 kb upstream of *Tsix*, including the minor *Tsix* promoter[45], the *Xite* enhancer region (see below for details on exact annotation)[44,45], the H3K27ac, H3K4me1, p300 enriched regions and the DNase I hypersensitive site, and it ends 53 bp before the end of the *Jpx* transcript (Supplementary Fig. 1a). These genomic inversions do not disrupt the sequence motifs of any of the known binding sites for pluripotency factors (Supplementary Fig. 1a), including REX1, the target of RNF12 (ref. [63]), and do not affect CTCF binding in the region (Supplementary Fig. 1b).

In UCSC RefSeq annotation[61], *Tsix* is annotated with the minor upstream promoter, while transcriptome analysis shows *Tsix* to be transcribed from the main downstream promoter only. *Xite* is not annotated at all in UCSC RefSeq annotation. Originally, *Xite* was annotated on the basis of a deletion (ΔL) covering chrX:100621540–100634048 mm9 (ref. [44]). *Xite* has often been annotated as the region in between the minor and major *Tsix* promoter. This annotation overlaps with the downstream part of the original annotation which has been shown to contain enhancer potential, while the upstream part has not[44]. This annotation runs up to the major *Tsix* promoter and includes a pair of CBSs, while the original annotation ends just before this pair of CBSs. Both annotations include the XhoI-StuI fragment that is required for the enhancer potential of *Xite*[45]. In this study, *Xite* has been depicted from the minor to the major *Tsix* promoter, including the pair of CBSs (*XiteC* in this study) and the enhancer activity containing XhoI-StuI fragment (*XiteE* in this study).

mESC culture and differentiation. Feeder-independent mouse ESCs (male: E14Tg2a.4; female: Pgk no. 106) were cultured on gelatin-coated flasks. Male (E14Tg2a.4) cells were grown in Glasgow medium supplemented with 2 mM L-Glutamine, 0.1 mM NEAA and 1 mM sodium pyruvate (GIBCO). Female (Pgk no. 106) cells were grown in DMEM (GIBCO). Both media contained 15% FBS (GIBCO), 10 M β-mercaptoethanol (Sigma) and 1,000 U ml^{-1} of leukemia inhibitory factor (Chemicon). Cells were cultivated in 8% CO_2. Male E14Tg2a.4 cells were obtained from the Sanger Institute. E14Tg2a.4 is a subclone of E14Tg2a. E14Tg2a cells were derived from the 129P2 mouse strain and Hprt mutated[64]. Female Pgk no. 106 were derived from Pgk12.1 (ref. [65]) and contain a heterozygote tetO knock-in allele, as described previously[66].

Before mESC to EpiLSC induction, female mESCs were grown for 2 d in medium as described above, supplemented with 3 μM GSK3 inhibitor (CT-99021) and 1 μM MEK1 inhibitor (PD-0325901). To induce mESCs into EpiLSCs[54,55], cells were plated on fibronectin coated six-well plates (10 μg ml^{-1} in PBS, Chemicon FC010) and grown in N2B27 medium (Stem Cell Sciences) supplemented with 10 ng ml^{-1} Fgf2 (R&D) and 20 ng ml^{-1} Activin A (R&D) at a cell density of 200,000 cells cm^{-2}. Cells were grown for 2 or 4 d, while refreshing the medium every day. For day 10 EpiLSCs, cells were plated as described above. At day 2, cells were incubated with JAK inhibitor (Calbiochem) for 24 h. Cells were split at day 3, day 5 and day 8 and collected for analysis at day 10.

Plasmids. Single guide RNAs were designed at each side of the region to be deleted or inverted, and cloned by annealing oligo pairs in pX330 for Cas9 nuclease, pX335 for Cas9 nickase and pX459 for Cas9 nuclease with Puromycin selection marker, according to the protocol described in ref. [67]. pX330, pX335 and pX459 plasmids were a gift from F. Zhang: respectively, Addgene no. 42230 (ref. [67]), Addgene no. 42335 (ref. [67]) and Addgene no. 48139 (ref. [68]).

For *Xite* mutants a pair of transcription activator-like effector nucleases (TALENs) was designed on each side of the region to be deleted or inverted. For TALEN construction, the TALE Toolbox kit (Addgene) and the protocol described by Sanjana et al.[69] were used. TALEN backbones were modified to contain a CAG promoter instead of the default CMV (cytomegalovirus) promoter[49].

Single guide RNA and TALEN sequences and Cas9 plasmids for each cell line were used as listed in Supplementary Table 1.

Generation of mutant mESC lines. mESCs were transfected with CRISPR plasmids or TALENs by means of the Amaxa 4D Nucleofector system (Lonza) using the P3 Primary Cell 4D Nucleofector X Kit (V4XP-3024) and the CG-104 (for E14Tg2a) or CG-110 (for Pgk no. 106) programs. Five million cells were transfected with 5 μg of each CRISPR plasmid, resuspended and seeded at serial dilutions in 10 cm dishes to ensure optimal density for colony picking. Transfected cells were selected with Puromycin for 48 h, and grown for 8–10 d. Single colonies or pools of colonies were picked into 96-well plates. Genomic DNA was isolated in 96-well plates and used for PCR-based screening. The strategy was inspired on the Epigenesys protocol by Nora and Heard, described here: https://www.epigenesys.eu/en/protocols/genome-engineering/816-engineering-genomic-deletions-and-inversions-in-mouse-es-cells-using-custom-designed-nucleases. Positive clones were subsequently re-seeded at single-cell dilution in 96-well plates, followed by PCR screening to obtain mono-clonal colonies. The PCR product of the selected clones was Sanger-sequenced to determine the exact location and allele of the respective deletion or inversion. Wild type alleles were also sequenced, to ensure their integrity. Karyotypes of selected clones were checked by metaphase chromosome spreads. Coordinates (mm9) of the deletions and inversions, can be found in Supplementary Table 1 and sequencing results of the deletions and inversion boundaries can be found in Supplementary Fig. 8a,b.

5C—chromosome conformation capture. The 5C was performed as described in Nora et al. (with some modifications, see below)[14], which incorporates in situ ligation[5] and adopts a single-PCR strategy to construct 5C-sequencing libraries from the chromosome conformation capture (3C) template.

Crosslinking was performed as described previously[14] using 2% formaldehyde. For 3C, 10 million cells were lysed in 1 ml 10 mM Tris-HCl, pH 8.0, 10 mM NaCl 0.2% NP-40 for 15 min, pelleted at 4 °C and washed once with 1 ml lysis buffer. Cells were then resuspended in a 1.5 ml tube in 100 μl 0.5% SDS in water, incubated at 62 °C for 10 min and immediately supplemented with 50 μl 10% Triton X-100 and 290 μl water, followed by incubation at 37 °C for 15 min. For restriction digestion, 50 μl 10× NEB2 buffer was added to the samples. Next, 50 μl was taken as an undigested control before adding 1,000 U of HindIII (high-concentration, NEB) for overnight incubation in a thermomixer at 1,400 r.p.m. The next morning, cells were incubated for 20 min at 65 °C, cooled at room temperature and 20 μl was taken as a digestion control. Ligation buffer and 10 U T4 ligase (Thermo Fisher catalog no. 15224) were added and after 4 h incubation at 25 °C in a thermomixer at 1,000 r.p.m., nuclei were centrifuged at 2,000 r.p.m., resuspended in 240 μl of 5% SDS and 1 mg Proteinase K, incubated at 55 °C for 30 min, supplemented with 50 μl 5 M NaCl and incubated at 65 °C for 4 h. DNA was then purified by adding 500 μl isopropanol, incubated at −80 °C overnight, centrifuged at 12,000 r.p.m. at 4 °C, washed with 70% ethanol, air dried and resuspended in 100 μl water, followed by incubation with RNase A at 37 °C. 3C templates were quantified using Qubit DNA Broad-Range (Thermo Fisher) and diluted to 100 ng μl^{-1}.

For 5 C we used the set of oligonucleotides described in ref. [3]. Four 10 μl 5C annealing reactions were assembled in parallel, each using 500 ng of 3C template, 1 μg salmon sperm (Thermo Fisher), 10 fmol of each 5C oligonucleotide in 1× NEBuffer 4. Samples were denatured at 95 °C for 5 min and incubated at 48 °C for 16–18 h. 10 μl of 1× Taq ligase buffer with 5 U Taq ligase were added to each annealing reaction followed by incubation at 48 °C for 4 h and 65 °C for 10 min. Negative controls (no ligase, no template, no 5C oligonucleotide) were included during each experiment to ensure the absence of contamination. To attach Illumina-compatible sequences, 5C libraries were directly PCR-amplified with primers harboring 50-mer tails containing Illumina sequences[14] that anneal to the universal T3/T7 portion of the 5C oligonucleotides. For this, each 5C ligation reaction was used as the template for three parallel PCRs (12 PCRs total), using per reaction 6 μl of 5C ligation with 1.125 U AmpliTaq Gold (Thermo Fisher) in 1× PCR buffer II, 1.8 mM $MgCl_2$, 0.2 mM dNTPs, 1.25 mM primers in 25 ml total. Cycling conditions were 95 °C for 9 min, 25 cycles of 95 °C for 30 s, 60 °C for 30 s, 72 °C for 30 s followed by 72 °C for 8 min. PCR products from the same 3C sample were pooled and run on a 2.0% agarose electrophoresis gel. Then, 5C libraries (231 bp) were then excised and purified with the MinElute Gel Extraction kit (QIAGEN). Library concentrations were estimated using TapeStation (Agilent) and Qubit (Thermo Fisher), pooled and sequenced using 12 pM for the loading on rapid flow cells using the HiSeq 2500 system (Illumina). Sequencing mode was set as 20 dark cycles followed by 80 bases in single-end reads (SR80). Between 7.2 and 28 million reads were sequenced per library (see Supplementary Table 2).

5C analysis. Sequencing data were processed using our custom pipeline, 5C-Pro, available at https://github.com/bioinfo-pf-curie/5C-Pro. Briefly, single-end sequencing reads were first trimmed to remove Illumina adapters and aligned on an in silico reference of all pairs of forward and reverse primers using the bowtie2 software[70]. Aligned reads were then directly used to infer the number of contacts between pairs of forward and reverse primers, thus providing a 5C map at the primer resolution. On the basis of our previous experiments, inefficient primers were discarded from downstream analysis. Quality controls of the experiments were then performed using the HiTC BioConductor package[71].

Data from biological replicates were pooled (summed) and binned using a running median (window = 30 kb, final resolution = 6 kb). We normalized 5C interactions for the total number of reads and filtered out outlier probes and singletons, as previously described[3,72,73]. Insulation scores calculated according to Crane et al.[74]. We also developed a new method to exclude noisy interactions in the 5C maps, called the 'neighborhood coefficient of variation', available at https://github.com/zhanyinx/Coefficient_Variation. Considering that the chromatin fiber behaves as a polymer, the contact frequency of a given pair of genomic loci (for example i and j) cannot be very different from those of fragments $i \pm N$ and $j \pm N$ if N is smaller (or in the order of) than the persistence length of the chromatin fiber. Hence, a given pixel in the 5C map (which is proportional to the contact frequency between the two corresponding loci) can be defined as noisy if its numerical value is too different from those corresponding to neighboring interaction frequencies. To operatively assess the similarity of a given interaction with neighboring interactions, we calculated the coefficient of

variation of interactions (pixels in the 5C map) in a 10 × 10 square centered on every interaction. We then set out to discard pixels for which the corresponding coefficient of variation was bigger than a threshold.

Given that the distribution of the coefficient of variation of all 5C samples in this study is bimodal around coefficient of variation = 1 (Supplementary Fig. 2b), we set the coefficient of variation threshold to 1. Discarded interactions appear as gray pixels in the differential 5C maps. For differential analysis between two samples of interest (generally wild type versus mutant), we calculated the $\log_2$ ratio between the respective filtered maps, and/or determined the difference between *Z*-scores calculated for each individual map[73]. Samples corresponding to inversions of genomic regions were mapped to a virtually inverted map before analysis. Samples corresponding to deletions were corrected for the new distance between genomic elements; this distance-adjustment was performed along with the *Z*-score calculation.

Capture-C. Capture probes were designed using CapSequm[40]. Sequences and genomic coordinates of capture probes can be found in Supplementary Table 3. Capture-C was performed as described in ref. [41]. In short, cells were fixed in 2% formaldehyde, then 10 million cells were lysed in 10 mM Tris-HCl, pH 8, 10 mM NaCl, 0.2% NP-40, 1× complete protease inhibitor cocktail (Roche) and homogenized using a Dounce homogenizer. To prepare 3C templates, chromatin was reconstituted in 664 µl water, and 50 µl of sample were taken as an undigested control. To prepare for digestion, 80 µl of restriction buffer and 10 µl 20% SDS was added, and incubated for 1 h at 37 °C in a thermomixer at 1,400 r.p.m. Next, 66 µl 20% Triton X-100 was added and incubation was continued for 1 h. Digestion was performed overnight by adding 10 µl DpnII (NEB, 50,000 U ml^{-1}) for 3 h, followed by 10 µl DpnII overnight and another 10 µl DpnII the next morning for 3–4 h, at 37 °C in a thermomixer. Then, 100 µl was taken as an unligated control. Digests were heat inactivated, diluted by adding 500 µl water and ligated overnight with 8 µl T4 ligase (30 U µl^{-1} EL0013 Thermo Fisher Scientific) and 133 µl Ligation buffer at 16 °C in a thermomixer at 1,400 r.p.m. DNA was then purified by overnight Proteinase K (Thermo Fisher Scientific ELO0491) treatment at 65 °C, followed by phenol/chloroform and chloroform extraction and ethanol precipitation at −80 °C for 4 h.

Sequencing libraries were prepared from 6 µg of 3C library by sonication using an S220 focused ultrasonicator (Covaris) to 200 bp and indexed using NEBNext reagents (New England Biolabs) according to the manufacturer's protocol. Subsequently, 2 µg indexed sequencing library was enriched for fragments of interest by incubation with 13 pM of biotinylated oligonucleotides (Integrated DNA Technologies, Supplementary Table 3) using the SeqCap EZ system (no. 06953212001, Roche/NimbleGen) according to the manufacturer's instructions. Two rounds of captures of, respectively, 72 and 24 h were performed. In the case of multiple captures for the same viewpoints, capture reactions were pooled and volumes multiplied by the number of reactions. Library size was confirmed using TapeStation D1000 (Agilent) and DNA concentrations were determined using Qubit (Thermo Fisher Scientific).

Capture-C libraries were sequenced on a MiSeq instrument (Illumina) using 150 base paired-end reads (PE150). Between 2.0 and 9.4 million read pairs were sequenced per library (see Supplementary Table 2). Raw reads were first trimmed using the Trim Galore! pipeline (http://www.bioinformatics.babraham.ac.uk/projects/trim_galore/), and then processed using the HiC-Pro pipeline[75] (v.2.8.0), until the detection of valid interaction products. Interaction products including the viewpoint of choice were selected using the makeViewpoint HiC-Pro utility. For plotting, interactions within 1 kb around the viewpoint were excluded, after which interaction frequencies were normalized to the number of interactions per DpnII fragment per 10,000 total interactions within the analyzed region (chrX:100214149–101420149), followed by a running mean with a window size of seven DpnII fragments.

Directional Capture-C signals were calculated as the percentage of interactions occurring in the 5′ or 3′ landscapes at either side of the respective viewpoint, relative to the total number of interactions within the visualized window (chrX:100214149–101420149|mm9) after excluding the interactions within a 20 kb window around the viewpoint and normalized to the size of the 5′ or 3′ landscapes.

RNA expression analysis. For gene expression profiling, cells were lysed by using Trizol (Invitrogen), then RNA was isolated using Silica column purification (Qiagen RNAeasy Mini kit) including DNase treatment. Nanostring nCounter quantification[76] was performed using 500 ng of total RNA per sample on a custom expression Codeset (Supplementary Table 4). Positive controls were used for scaling of the raw data and the housekeeping genes *Actb*, *Rrm2* and *Sdha* were used for normalization. Expression data for the different mutants is always compared to a wild type that was processed on the same nCounter run.

For allelic expression analysis of *Xist*, complementary DNA was prepared using random priming with Superscript III (Life Technologies), followed by PCR amplification using primers with the following sequences: (Btn) AGAGAGCCCAAAGGGACAAA and TGTATAGGCTGCT GGCAGTCC. Successfully amplified PCR products from cDNA were purified and annealed with the pyrosequencing primer, GCTGGCAGTCCTTGA, and analyzed for the G/A SNP at mm9 position 100665998 using the PyroMark Q24 (Qiagen). PCR and sequencing primers were designed using the PyroMark Assay Design software.

RNA-seq libraries were prepared from 500 ng of DNase-treated total RNA (RNA integrity number > 7) with the TruSeq Stranded mRNA kit (Illumina). Sequencing was performed in using 100 base paired-end (PE100) reads using the Illumina HiSeq2000 platform (Supplementary Table 2). RNA sequencing reads have been aligned on the Mouse reference genome (mm9) using the STAR mapper (v.2.5.2b)[77] and the GENCODE (vM1) annotations[78], allowing up to six mismatches and reporting only unique hits. Reads counts per gene were also generated with STAR and combined across samples to generate the raw counts table. Gene counts were filtered to be >1 in at least two samples and normalized by the trimmed mean of M values (TMM) using the edgeR package[79,80]. Differential expression was determined using the EdgeR package[79,80]. X/A expression ratio as the level of expression of X-linked genes divided by the global level of expression of the autosomal genes was calculated as described in ref. [81]. Only genes with CPM > 1 in the wild type were used for this analysis.

RNA–FISH. RNA–FISH was performed as previously described[82], using probes specified in Supplementary Table 5. Three-dimensional image stacks were analyzed using custom-made ImageJ macros.

In brief, cells were dissociated using accutase and subsequently attached to poly-lysine (0.1% w/v in water) coated coverslips by 15 min incubation. Attached cells were washed in PBS and fixed in 3% paraformaldehyde for 10 min. Cells were permeabilized on ice for 5 min in 1× PBS, 0.5% Triton X-100 and 2 mM ribonucleoside vanadyl complex (NEB) and washed and stored in 70% ethanol at −20 °C. Before RNA–FISH, cells were dehydrated through washes with 80, 95, 100 and 100% ethanol. Nascent *Tsix* transcripts were detected with the pLG10 plasmid as probe[49], using 1 µg plasmid for nick translation. Genomic coordinates of sequences recognized by the pLG10 probe are chrX:100641751–100646253 (mm9). Xist RNA was detected using a custom designed strand-specific probe that covers all exons with ~75-bp-long oligonucleotides (chrX:100656573–100678635, mm9), which are end-labeled with the Alexa488 fluorophore (Roche). Per coverslip, 50 ng of labeled pLG10 and/or 100 ng of end-labeled oligonucleotides were ethanol-precipitated and (co)hybridized in FISH hybridization buffer (50% formamide, 20% dextran sulfate, 2× SSC, 1 µg µl^{-1} BSA, 10 mM ribonucleoside vanadyl complex) overnight at 37 °C. The next day, cells were washed at 42 °C three times for 5 min with 50% formamide/2× SCC at pH 7.3 and three times for 5 min with 2× SSC. Samples were counterstained with 0.2 mg ml^{-1} DAPI, washed two times for 5 min at room temperature with 2× SSC, and mounted with 90% glycerol, 0.1× PBS and 0.1% *p*-phenylenediamine (Sigma). Images were acquired on a DeltaVision widefield system, a minimum of 100 cells per clone per replicate were counted (Supplementary Table 6)

RAP coupled with DNA sequencing. A total of 5 million MESCs (E14, 40-kb or 70-kb inversion) were crosslinked with 2 mM disuccinimidyl glutarate and 3% formaldehyde. Cells were lysed and Xist RNA was purified as previously described[52]. Xist RNA was captured using antisense 5′ biotinyated 90-mer DNA probes, which spanned the *Xist* sequence. Captures were carried out as described previously[52]. Briefly, lysates were precleared with streptavidin magnetic beads for 30 min at 37 °C. After preclearing, supernatant was mixed with 1 µg of *Xist* probes and incubated at 37 °C for 2 h. A portion of this sample was retained as the input plus probe control. Probe-RNA hybrids were captured with streptavidin magnetic beads at 37 °C for 30 min. Beads were washed four times with GuSCN hybridization buffer (20 mM Tris-HCl pH 7.5, 7 mM EDTA, 3 mM EGTA, 150 mM LiCl, 1% NP-40, 0.2% N-lauroylsarcosine, 0.1% sodium deoxycholate, 3 M guanidine thiocyanate, 2.5 mM TCEP) followed by two washes with GuSCN wash buffer (20 mM Tris-HCl pH 7.5, 10 mM EDTA, 1% NP-40, 0.2% *N*-lauroylsarcosine, 0.1% sodium deoxycholate, 3 M guanidine thiocyanate, 2.5 mM TCEP). Captured DNA was eluted with 15 U RNase H in 20 µl RNase H buffer at 37 °C for 1 h, as previously described[52]. After elution, protein crosslinking was reversed for both capture and input plus probe samples, and DNA was prepared for Illumina sequencing using a NEBNext chromatin immunoprecipitation (ChIP)-Seq Library Prep kit. Capture efficiency was assessed by quantitative PCR (qPCR) for the Xist RNA in the elution relative to the input plus probe samples.

Sequencing alignment and analysis was carried out as previously described[52,83,84]. In brief, libraries were sequenced using 35-bp paired-end reads. Between 5.8 and 921.2 million read pairs were sequenced per library (see Supplementary Table 2). After sequencing, adapter indexes were trimmed from all reads and samples were aligned to the mouse genome (build: mm9). Duplicates were marked and removed using picard and these data were used for enrichment calculations across the X chromosome at 10-kb window sizes. All elution counts were normalized against input plus probe controls from their respective samples. In addition, mouse lung fibroblast data from GSE46918 was processed as above and used for enrichment calculations.

Chromatin immunoprecipitation. Cells were crosslinked as previously described[85]. Briefly, cells were initially fixed in 1.5 mM ethylene glycolbis(succinimidyl succinate) (EGS); next 1% formaldehyde was added and further incubated for 10 min. After rinsing twice in PBS, cells were scraped and pellets snap frozen. Fixed pellets were lysed in 2 ml nuclear lysis buffer (0.5% Triton X-100, 0.1 M sucrose, 5 mM $MgCl_2$, 1 mM EDTA, 10 mM Tris-HCl pH 8.0,

1× protease inhibitors) for 10 min on ice and douce-homogenized. Nuclei were pelleted and resuspended in 0.3 ml lysis buffer (1 mM EDTA, 0.5 mM EGTA, 10 mM Tris pH 8.0, 0.5% *N*-lauroylsarcosine, 1× protease inhibitors). Chromatin was sheered using a BioruptorPlus (Diagenode) set to high for 30 cycles. Unsonicated chromatin was removed by centrifugation. Supernatant was diluted with 1.2 ml of dilution buffer (1.25% Triton, 0.125% sodium deoxycholate, 6 mM EDTA, 10 mM Tris-HCl pH 8.0, 1× protease inhibitors) and antibody coated beads were added (per immunoprecipitation: 8 µl of anti-CTCF antibody (Active Motif, no. 61311) and 40 µl of Protein-A dynabeads). Samples were left rotating overnight at 4 °C. The following day, beads were magnet-separated and washed four times with Low Salt Buffer (0.1% SDS; 1% Triton X-100; 2 mM EDTA; 20 mM Tris-HCl, pH 8.1; 150 mM NaCl; 0.1% sodium deoxycholate), twice with High Salt Buffer (0.1% SDS; 1% Triton X-100; 2 mM EDTA; 20 mM Tris-HCl, pH 8.1; 360 mM NaCl; 0.1% sodium deoxycholate) and twice with LiCl buffer (0.25 M LiCl; 1% NP-40; 1.1% sodium deoxycholate; 1 mM EDTA; 10 mM Tris-HCl pH 8.1). Before elution, all samples were rinsed once in Tris-EDTA buffer. ChIP–DNA was eluted in ProtK-Digestion Buffer (20 mM HEPES; 1 mM EDTA; 0.5% SDS; 0.8 mg ml^{-1} Proteinase K) for 15 min at 56 °C. Beads were separated and the supernatant was further digested for another 2 h at 56 °C and then decrosslinked for 4 h at 68 °C. DNA was isolated using AMPure XP beads. Samples were quantified in triplicates using real-time qPCR and enrichments were normalized to the ChIP input sample as well as a positive enrichment control CBS region. Primer sequences are available in Supplementary Table 7.

Statistics. Statistical analysis of inter-TAD interactions was performed using a two-sample, two-tailed heteroscedastic *t*-test. Statistical analysis of Xist RNA–FISH experiments in male cell lines was performed using one-sided Welch's *t*-tests, using the *t*-test from the R stats package. *P* values were adjusted for multiple testing by Benjamini–Hochberg correction, using p.adjust from the R stats package. Statistical differences between mutant and wild type Xist RAP enrichment or X-linked gene silencing were determined by two-sided Wilcoxon rank sum tests, using wilcox.test from the R stats package. Statistical analysis of Xist RNA–FISH experiments in female cell lines was carried out on independent experiments by two-sided Fisher's exact tests, using fisher.test from the R stats package. Bi-allelic *Tsix* expression measured by RNA–FISH in the female cell lines was tested for statistical significance on independent experiments by Pearson's chi-squared tests with Yates' continuity correction, using chisq.test from the R stats package. Statistical analysis of reduced and dispersed Xist RNA cloud formation in mutant female cell lines that expresses Tsix RNA from one or neither X chromosome versus both X chromosomes was carried out on each independent experiment using a two-sided Fisher's exact test using fisher.test from the R stats package. *P* values for differentially expressed genes measured by RNA sequencing were calculated with gene-wise exact tests for differences in the means between two groups of negative-binomially distributed counts, using exactTest from the R stats package R. *P* values were corrected for multiple testing by a Benjamini–Hochberg correction, using p.adjust from the R stats package.

Reporting Summary. Further information on research design is available in the Nature Research Reporting Summary linked to this article.

Data availability

Data have been deposited in the NCBI GEO under the accession number GSE111205. Reagents, cell lines and other data supporting the findings of this study are available from the corresponding author upon request.

Code availability

Our custom pipeline for 5C data processing, 5C-Pro, is available at https://github.com/bioinfo-pf-curie/5C-Pro. Custom codes used in this study will be provided upon request.

References

62. Pillet, N., Bonny, C. & Schorderet, D. F. Characterization of the promoter region of the mouse Xist gene. *Proc. Natl Acad. Sci. USA* **92**, 12515–12519 (1995).
63. Gontan, C. et al. RNF12 initiates X-chromosome inactivation by targeting REX1 for degradation. *Nature* **485**, 386–390 (2012).
64. Doetschman, T. et al. Targetted correction of a mutant HPRT gene in mouse embryonic stem cells. *Nature* **330**, 576–578 (1987).
65. Norris, D. P. et al. Evidence that random and imprinted Xist expression is controlled by preemptive methylation. *Cell* **77**, 41–51 (1994).
66. Masui, O. et al. Live-cell chromosome dynamics and outcome of X chromosome pairing events during ES cell differentiation. *Cell* **145**, 447–458 (2011).
67. Cong, L. et al. Multiplex genome engineering using CRISPR/Cas systems. *Science* **339**, 819–823 (2013).
68. Ran, F. A. et al. Genome engineering using the CRISPR-Cas9 system. *Nat. Protoc.* **8**, 2281–2308 (2013).
69. Sanjana, N. E. et al. A transcription activator-like effector toolbox for genome engineering. *Nat. Protoc.* **7**, 171–192 (2012).
70. Langmead, B. & Salzberg, S. L. Fast gapped-read alignment with Bowtie 2. *Nat. Methods* **9**, 357–359 (2012).
71. Servant, N. et al. HiTC: exploration of high-throughput 'C' experiments. *Bioinformatics* **28**, 2843–2844 (2012).
72. Hnisz, D. et al. Activation of proto-oncogenes by disruption of chromosome neighborhoods. *Science* **351**, 1454–1458 (2016).
73. Smith, E. M., Lajoie, B. R., Jain, G. & Dekker, J. Invariant TAD boundaries constrain cell-type-specific looping interactions between promoters and distal elements around the CFTR Locus. *Am. J. Hum. Genet.* **98**, 185–201 (2016).
74. Crane, E. et al. Condensin-driven remodelling of X chromosome topology during dosage compensation. *Nature* **523**, 240–244 (2015).
75. Servant, N. et al. HiC-Pro: an optimized and flexible pipeline for Hi-C data processing. *Genome Biol.* **16**, 259 (2015).
76. Geiss, G. K. et al. Direct multiplexed measurement of gene expression with color-coded probe pairs. *Nat. Biotechnol.* **26**, 317–325 (2008).
77. Dobin, A. et al. STAR: ultrafast universal RNA-seq aligner. *Bioinformatics* **29**, 15–21 (2013).
78. Mudge, J. M. & Harrow, J. Creating reference gene annotation for the mouse C57BL6/J genome assembly. *Mamm. Genome* **26**, 366–378 (2015).
79. Robinson, M. D., McCarthy, D. J. & Smyth, G. K. edgeR: a Bioconductor package for differential expression analysis of digital gene expression data. *Bioinformatics* **26**, 139–140 (2010).
80. McCarthy, D. J., Chen, Y. & Smyth, G. K. Differential expression analysis of multifactor RNA-Seq experiments with respect to biological variation. *Nucleic Acids Res.* **40**, 4288–4297 (2012).
81. Borensztein, M. et al. Xist-dependent imprinted X inactivation and the early developmental consequences of its failure. *Nat. Struct. Mol. Biol.* **24**, 226–233 (2017).
82. Chaumeil, J., Augui, S., Chow, J. C. & Heard, E. Combined immunofluorescence, RNA fluorescent in situ hybridization, and DNA fluorescent in situ hybridization to study chromatin changes, transcriptional activity, nuclear organization, and X-chromosome inactivation. *Methods Mol. Biol.* **463**, 297–308 (2008).
83. Engreitz, J. M. et al. RNA-RNA interactions enable specific targeting of noncoding RNAs to nascent pre-mRNAs and chromatin sites. *Cell* **159**, 188–199 (2014).
84. Chen, C. K. et al. Xist recruits the X chromosome to the nuclear lamina to enable chromosome-wide silencing. *Science* **354**, 468–472 (2016).
85. Zeng, P. Y., Vakoc, C. R., Chen, Z. C., Blobel, G. A. & Berger, S. L. In vivo dual cross-linking for identification of indirect DNA-associated proteins by chromatin immunoprecipitation. *Biotechniques* **41**, 696–698 (2006).

nature research

Corresponding author(s): Edith Heard, Joke van Bemmel

Reporting Summary

Nature Research wishes to improve the reproducibility of the work that we publish. This form provides structure for consistency and transparency in reporting. For further information on Nature Research policies, see Authors & Referees and the Editorial Policy Checklist.

Statistical parameters

When statistical analyses are reported, confirm that the following items are present in the relevant location (e.g. figure legend, table legend, main text, or Methods section).

n/a	Confirmed	
☐	☒	The exact sample size (*n*) for each experimental group/condition, given as a discrete number and unit of measurement
☐	☒	An indication of whether measurements were taken from distinct samples or whether the same sample was measured repeatedly
☐	☒	The statistical test(s) used AND whether they are one- or two-sided *Only common tests should be described solely by name; describe more complex techniques in the Methods section.*
☒	☐	A description of all covariates tested
☒	☐	A description of any assumptions or corrections, such as tests of normality and adjustment for multiple comparisons
☒	☐	A full description of the statistics including central tendency (e.g. means) or other basic estimates (e.g. regression coefficient) AND variation (e.g. standard deviation) or associated estimates of uncertainty (e.g. confidence intervals)
☒	☐	For null hypothesis testing, the test statistic (e.g. *F*, *t*, *r*) with confidence intervals, effect sizes, degrees of freedom and *P* value noted *Give P values as exact values whenever suitable.*
☒	☐	For Bayesian analysis, information on the choice of priors and Markov chain Monte Carlo settings
☒	☐	For hierarchical and complex designs, identification of the appropriate level for tests and full reporting of outcomes
☒	☐	Estimates of effect sizes (e.g. Cohen's *d*, Pearson's *r*), indicating how they were calculated
☐	☒	Clearly defined error bars *State explicitly what error bars represent (e.g. SD, SE, CI)*

Our web collection on statistics for biologists may be useful.

Software and code

Policy information about availability of computer code

Data collection	No custom code was used for data collection
Data analysis	5C sequencing data was processed using 5C-Pro (https://github.com/bioinfo-pf-curie/5C-Pro), quality controls were performed using the HiTC BioConductor package, noisy interactions were excluded using "neighborhood coefficient of variation" (https://github.com/zhanyinx/Coefficient_Variation). Capture-C sequencing reads were trimmed using the Trim Galore! pipeline (http://www.bioinformatics.babraham.ac.uk/projects/trim_galore/), processed using the HiC-Pro pipeline (v2.8.0) and informative interactions were selected using the makeViewpoint HiC-Pro utility. RNA sequencing reads were aligned using the STAR mapper (v2.5.2b) and the GENCODE (vM1) annotations, reads counts per gene were generated with STAR. Read counts were normalized and analyzed for differential expression using the EdgeR package. RAP sequencing reads were aligned using BWA version 0.5.9, and filtered using Picard.

For manuscripts utilizing custom algorithms or software that are central to the research but not yet described in published literature, software must be made available to editors/reviewers upon request. We strongly encourage code deposition in a community repository (e.g. GitHub). See the Nature Research guidelines for submitting code & software for further information.

Data

Policy information about availability of data

All manuscripts must include a data availability statement. This statement should provide the following information, where applicable:

- Accession codes, unique identifiers, or web links for publicly available datasets
- A list of figures that have associated raw data
- A description of any restrictions on data availability

Data has been deposited in the NCBI GEO under the accession number GSE111205. This data is associated to main Figures 1, 2, 3 and 4, and to Supplementary Figures 2, 3, 4, 5 and 6.

Field-specific reporting

Please select the best fit for your research. If you are not sure, read the appropriate sections before making your selection.

☒ Life sciences ☐ Behavioural & social sciences

For a reference copy of the document with all sections, see nature.com/authors/policies/ReportingSummary-flat.pdf

Life sciences

Study design

All studies must disclose on these points even when the disclosure is negative.

Sample size	No sample-size calculation was performed. Sample size for one biological replicate for DNA or RNA FISH experiments presented in this study was usually n>100. These numbers for single cell quantitative or qualitative analysis are common in the field.
Data exclusions	Based on our previous experiments (Nora et al 2012), inefficient primers in the 5C analysis were discarded prior to downstream analysis.
Replication	All experiments have been replicated at least twice, and all attempts of replication were successful. Replicates were performed by using an independently generated cell line and/or by repeating the experiment on the same cell line. Replicates on the same cell line were performed on independently cultured cell passages. Specifics for each experiment have been detailed in text and figure legends, in short: 5C experiments were performed twice for each cell line (replicates were pooled) with two cell lines for each genomic alteration, except for cell line 13b and D7 for which 5C was performed once; Capture-C experiments were performed once for each independent cell line; RNAseq was performed twice for each cell line, with two cell lines for each inversion; RAP was performed twice for each cell line, with one cell line for each inversion; FISH was performed at least twice for each cell line, with two cell lines for each male inversion and one for each female; nCounter analysis was performed twice for each cell line, with two cell lines for each male inversion and one for each female inversion; Pyrosequencing was performed twice on each cell line, with one cell line for each female.
Randomization	Not relevant, since experimental groups were based on genotypes.
Blinding	For key conclusions, counting of RNA FISH images was repeated blindly by an another person.

Materials & experimental systems

Policy information about availability of materials

n/a	Involved in the study
☒	☐ Unique materials
☒	☐ Antibodies
☐	☒ Eukaryotic cell lines
☒	☐ Research animals
☒	☐ Human research participants

Eukaryotic cell lines

Policy information about cell lines

Cell line source(s)	Parental wildtype male mESCs, E14Tg2a.4, were obtained from Sanger. E14Tg2a.4 is a subclone of E14Tg2a. E14Tg2a cells were derived from the 129P2 mouse strain and Hprt mutated (Doetschman et al. Nature, 1987). Female mESCs, Pgk#106, were derived from Pgk12.1 and contain a heterozygote tetO knock-in allele (Masui et al. Cell, 2011). Pgk12.1 originates from Norris et al. Cell, 1994.
Authentication	No authentication performed on source cell lines. Cell lines generated in this study were validated using PCR and Sanger sequencing.

Mycoplasma contamination	All cell lines tested negative for Mycoplasma contamination.
Commonly misidentified lines (See ICLAC register)	None of the cell lines used are listed in the ICLAC database.

Method-specific reporting

n/a	Involved in the study
☒	☐ ChIP-seq
☒	☐ Flow cytometry
☒	☐ Magnetic resonance imaging